remote sensing

MDPI

Article

A Framework for Winter Wheat Soil Moisture Retrieval Based on UAV Remote Sensing and AutoML

Daokuan Zhong [1,2,†], Caixia Li [2,†], Shenglin Li [3], James E. Kanneh [2], Pengyuan Zhu [2], Hao Liu [2], Ni Song [2], Huifeng Ning [2] and Chitao Sun [1,*]

[1] College of Water Conservancy and Civil Engineering, Shandong Agricultural University, Taian 271018, China; 2023121344@sdau.edu.cn
[2] Key Laboratory of Crop Water Use and Regulation, Ministry of Agriculture and Rural Affairs, Farmland Irrigation Research Institute, Chinese Academy of Agricultural Sciences, Xinxiang 453002, China; licaixia@caas.cn (C.L.); 2023y90200009@caas.cn (J.E.K.); 82101232120@caas.cn (P.Z.); songni@caas.cn (N.S.); ninghuifeng@caas.cn (H.N.)
[3] School of Information Engineering, Henan Institute of Science and Technology, Xinxiang 453003, China; shenglinli@hist.edu.cn
* Correspondence: chitaosun@sdau.com
† These authors contributed equally to this work.

Highlights

What are the main findings?

- Novel dual-band and three-band hyperspectral indices were constructed, and the H2O AutoML model achieved the highest accuracy ($R \geq 0.72$) for estimating soil moisture at 0–40 cm depths.
- Fusing Hyperspectral, Thermal Infrared, and RGB data yielded the best performance, with the Thermal Vegetation Dryness Index (TVDI) identified as the most critical feature for retrieval.

What are the implications of the main findings?

- The proposed framework integrates multi-source UAV remote sensing with automated machine learning, providing a robust technical approach for precise agricultural water resource management.
- This method effectively overcomes single-sensor limitations, offering a scalable solution for monitoring regional soil moisture dynamics in winter wheat fields.

Abstract

Soil moisture content (SMC) is a critical factor in agricultural management; however, traditional monitoring methods face limitations regarding spatial resolution and the acquisition of regional dynamics. Unmanned Aerial Vehicle (UAV) remote sensing offers new opportunities for precision monitoring. This study proposes a UAV-based multi-modal remote sensing method for soil moisture estimation. Specifically, novel dual-band and three-band hyperspectral (HS) indices were constructed, and visible (RGB) and thermal infrared (TIR) information were integrated to form a multi-modal data system; simultaneously, multi-modal estimation models were developed by combining four AutoML methods: TPOT, AutoGluon, H2O AutoML, and FLAML. The results indicate that the H2O AutoML model, fusing multi-modal data, exhibited the best performance in estimating soil moisture at depths of 0–20 cm and 20–40 cm ($R \geq 0.72$, RMSE 1.99–2.17%), demonstrating superior stability and generalization capabilities compared to other models. This study has made progress in hyperspectral index construction, multi-modal fusion, and soil moisture retrieval, providing a new technical approach for the refined management of agricultural water resources.

Check for updates

Academic Editor: Luca Brocca

Received: 10 February 2026
Revised: 1 April 2026
Accepted: 7 April 2026
Published: 12 April 2026

Copyright: © 2026 by the authors. Licensee MDPI, Basel, Switzerland. This article is an open access article distributed under the terms and conditions of the Creative Commons Attribution (CC BY) license.

Keywords: soil moisture content; UAV; multi-source remote sensing; hyperspectral index; automated machine learning

1. Introduction

Soil moisture content (SMC) plays a crucial regulatory role in wheat growth and agricultural production [1], and it is essential for ensuring food security, optimizing irrigation decisions, and improving water use efficiency [2]. Driven by various environmental factors such as temperature, evapotranspiration, and precipitation, the spatiotemporal variability of SMC is complex and dynamic, making it a long-standing challenge in agricultural monitoring [3]. Therefore, developing an efficient, accurate, and scalable SMC monitoring method is of great significance for improving agricultural productivity and the rational utilization of water resources. Currently, methods for acquiring SMC at the regional scale include ground point measurements, Unmanned Aerial Vehicle (UAV) remote sensing, satellite remote sensing, and data assimilation methods [4]. Although ground measurements offer high accuracy, their spatial coverage is limited, and they are labor- and material-intensive, making large-scale monitoring difficult. While satellite remote sensing provides extensive soil moisture data coverage [5], it is limited by low spatial resolution as well as the effects of weather and revisit cycles, which hinders the timely monitoring of SMC changes [6]. Recently, Global Navigation Satellite System-Reflectometry (GNSS-R), such as the CYGNSS mission, has emerged as a powerful tool to overcome these limitations. Although possessing coarser spatial resolution than UAVs, CYGNSS provides frequent revisit times and cloud-penetrating capabilities, offering a pathway for scaling up surface soil moisture monitoring to regional or global levels. Furthermore, recent advancements in deep learning, particularly the application of Vision Transformer (ViT) models, have shown great promise in efficiently processing CYGNSS data for large-scale soil moisture estimation [7,8]. Although data assimilation methods have advantages in timeliness, their spatial resolution remains limited by the resolution of the remote sensing input data, failing to meet the needs of precision monitoring at the field scale [9]. In contrast, UAV-based remote sensing technology has become a powerful tool for SMC estimation due to its high spatiotemporal resolution, controllable revisit cycle, and ability to carry multiple sensors [10,11]. UAVs can be flexibly equipped with multispectral (MS), hyperspectral (HS), and thermal infrared (TIR) sensors according to research needs, and flight altitude and time can be adjusted to acquire high-quality, high-resolution remote sensing data [2,3].

Physiologically, water stress reduces leaf water content, induces stomatal closure, and alters chlorophyll concentration. When crop roots struggle to absorb sufficient water from the soil, plant water potential decreases, significantly affecting the crop's spectral reflectance characteristics and subsequently leading to a decrease in Normalized Difference Vegetation Index (NDVI) values [12]. Therefore, crop water deficit status can be identified by capturing changes in spectral characteristics and related indices, thereby indirectly predicting SMC changes at the regional scale. In recent years, traditional machine learning algorithms such as Support Vector Regression (SVR), Random Forest (RF), and Artificial Neural Networks (ANN) have shown potential in SMC estimation [13,14]. For example, relevant studies have utilized SVR and RF to achieve high-precision retrieval of soil moisture in maize canopies and citrus orchards [15], respectively, while other scholars have achieved dynamic monitoring of farmland SMC using ANN [16]. Although these methods have achieved certain results, they typically require extensive manual parameter fine-tuning for specific datasets, and a single model structure often struggles to adapt to the complexity of multi-modal data, leading to limited model generalization ability. In contrast, AutoML can intelligently

search for the optimal combination of algorithms and parameters, significantly improving the accuracy and robustness of SMC prediction models while reducing dependence on expert prior knowledge.

Furthermore, most existing studies rely on multispectral data with limited bands, which is insufficient to capture fine differences in SMC changes, especially for high-precision estimation of root zone SMC. The development of airborne remote sensing sensors has provided multi-source and multi-dimensional data for SMC estimation [17]. Hyperspectral remote sensing, with its continuous and narrow band characteristics, can reveal subtle differences in the spectral response of soil and vegetation, offering unique advantages in detecting SMC changes [18]. RGB images provide high-resolution texture and structure information, helping to reflect land cover distribution and crop growth status, serving as a direct auxiliary data source for SMC estimation. Thermal infrared remote sensing captures land surface temperature and reflects the evapotranspiration process, enabling indirect monitoring of SMC, with particularly strong sensitivity under drought conditions [19]. Therefore, a key scientific issue in precision agriculture is how to design effective multi-modal data fusion strategies at the regional scale to fully utilize the complementary information of HS, RGB, and TIR data, thereby improving the accuracy and robustness of root zone SMC estimation [20,21]. Based on this background, this study utilized a UAV equipped with HS, RGB, and TIR sensors, combined with four advanced automated machine learning models (TPOT, AutoGluon, H2O AutoML, and FLAML), to estimate SMC at depths of 0–20 cm and 20–40 cm in wheat fields. By selecting hyperspectral bands and constructing novel indices, this study aims to enhance the sensitivity of the models to SMC and improve estimation accuracy, providing a new method for precision SMC monitoring at the field scale.

2. Materials and Methods

2.1. Study Area

This study was conducted from April to May 2024 at the Xinxiang Comprehensive Experimental Base of the Chinese Academy of Agricultural Sciences (35°18′11″N, 113°55′34″E) (Figure 1). The experimental station is located in Xinxiang City, Henan Province, with an average altitude of 73.3 m, and is characterized by a typical temperate continental monsoon climate. The mean annual temperature in the region is 14.5 °C, and the mean annual precipitation is 573.4 mm, with an uneven spatiotemporal distribution mainly concentrated in the summer. The region has a frost-free period of approximately 205 days per year, and historical extreme temperatures range from −19.2 °C to 42.0 °C. The soil type in the experimental area is primarily brown soil, characterized by good water retention and fertility. This region is an important production base for high-quality wheat in China, mainly implementing a winter wheat–summer maize double cropping system.

2.2. Data Collection and Preprocessing

2.2.1. UAV Data Acquisition

In this study, a DJI M-300 RTK UAV (SZ DJI Technology Co., Ltd., Shenzhen, China) equipped with multi-modal sensors was used to collect remote sensing data during the winter wheat growing season. The primary payloads included: (1) a Pika L HS imager (Resonon Inc., Bozeman, MT, USA), covering the 400–1000 nm spectral range with a spectral resolution of 2.7 nm (150 bands in total); and (2) a Zenmuse XT-2 dual-sensor camera (SZ DJI Technology Co., Ltd., Shenzhen, China), used to synchronously acquire high-resolution RGB images and TIR canopy temperature information (Figure 2). Detailed parameters of the sensors are shown in Table 1. Data acquisition covered the key growth stages of winter wheat in 2024, with specific dates being 17 April (heading stage), 22 April (flowering

stage), 1 May (early grain-filling stage), 10 May (mid grain-filling stage), and 17 May (late grain-filling stage). These stage assignments were determined based on field observations and regional phenological characteristics of winter wheat in Henan Province. All flight missions were scheduled between 10:00 and 14:00 under clear and cloudless conditions to ensure a high solar elevation angle and stable lighting conditions. To balance the trade-off between spatial resolution and the need to capture the entire 40 ha study area within this strict temporal window of stable illumination, the flight altitude was uniformly set to 400 m. At this altitude, 9 flight lines were planned to cover the entire area efficiently, minimizing battery replacements and avoiding temporal drift in thermal and spectral responses. Specifically, the HS flight speed was 10 m/s, with forward and side overlaps of 70% and 75%, respectively; the XT-2 flight speed was 8 m/s, with overlaps set at 75% and 80%. Five fixed Ground Control Points (GCPs) were deployed in the study area for geometric correction and multi-temporal registration.

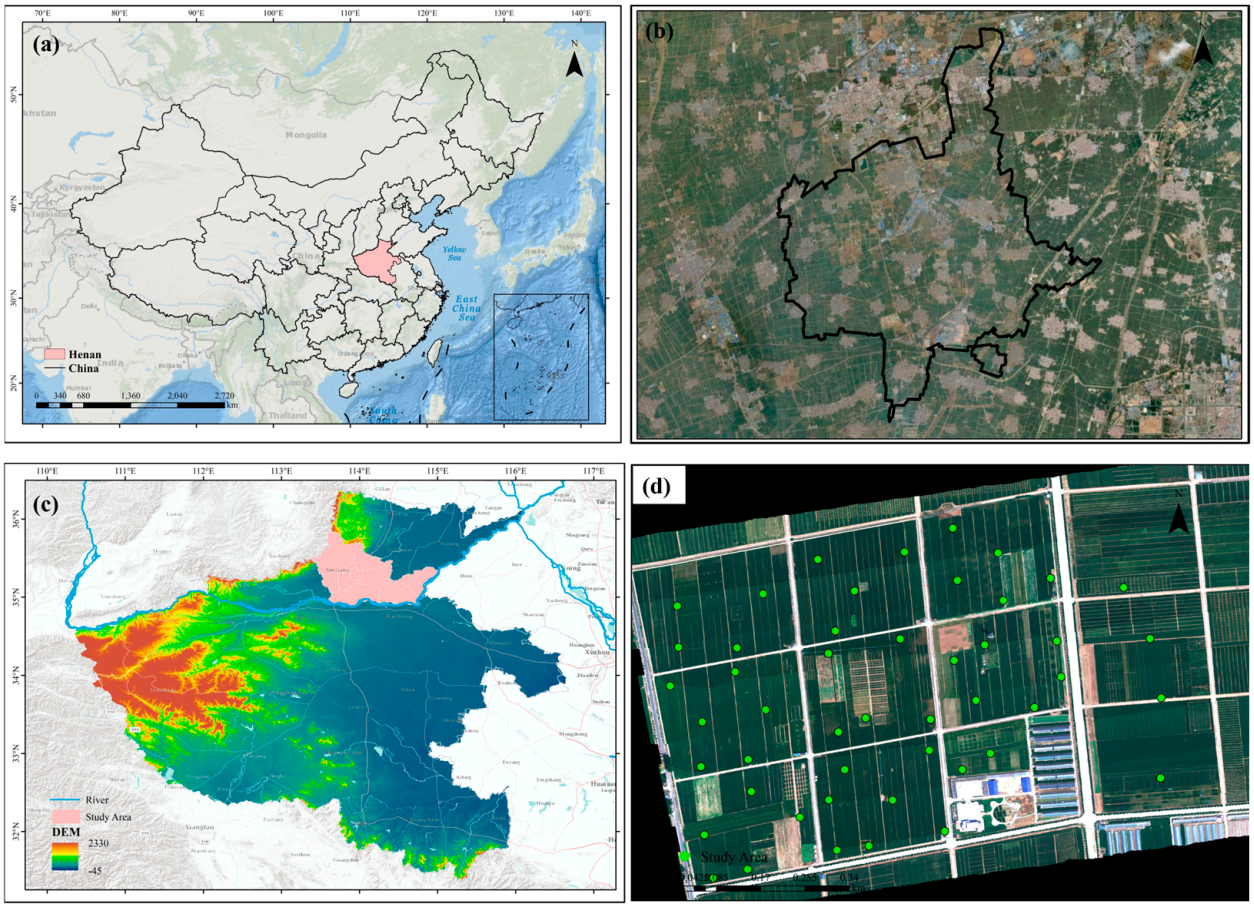


Figure 1. Overview of the study area. (**a**,**b**) show the geographic location of the experimental area; (**c**) distribution of SMC sampling points; (**d**) spatial distribution of sampling points in the study area. The green dots indicate the soil sampling points.

Table 1. Sensor specifications of the UAV platform.

Sensor Name	Sensor Type	Spectral Range	Spectral Resolution	Resolution	Focal Length
Zenmuse XT2	RGB	400–700 nm	N/A	4000 × 3000 pixels (12 MP)	8 mm
	TIR	7.5–13.5 um	N/A	640 × 512 pixels	19 mm
Pika L	HS	400–1000 nm	2.7 nm	900 spatial pixels	17 mm

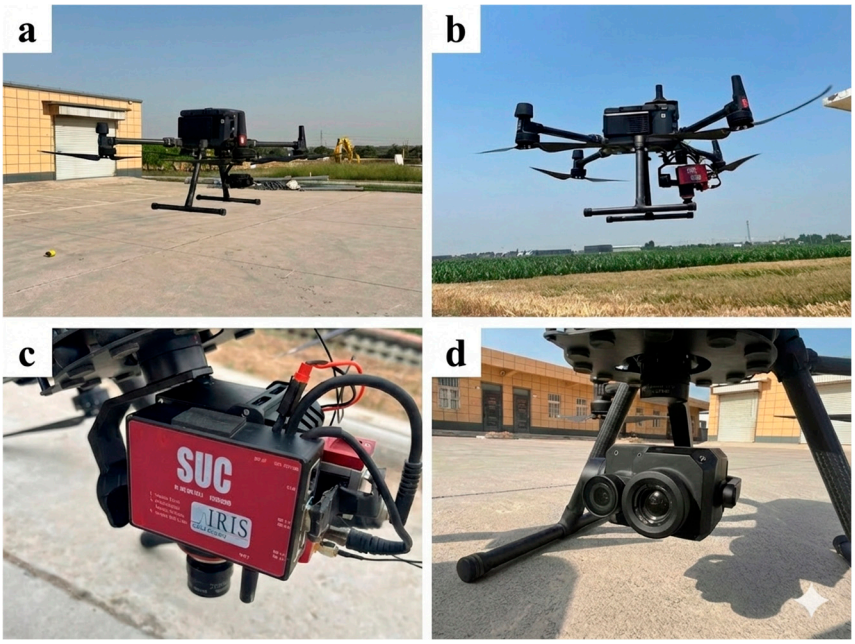


Figure 2. UAV platform and onboard HS and TIR sensors. (**a**,**b**) DJI M300 UAV; (**c**) HS camera; (**d**) RGB and TIR camera.

2.2.2. Ground-Based Soil Moisture Content Data Collection

To ensure synchronization between ground SMC sampling and UAV flights, 50 GPS-located sampling points were selected within the study area. Soil samples were collected at depths of 0–20 cm and 20–40 cm, as these two layers represent functionally important portions of the winter wheat root zone. Specifically, the 0–20 cm layer corresponds to the shallow active root zone, where roots are highly concentrated and soil moisture is more directly linked to near-surface thermal and spectral responses. The 20–40 cm layer represents a deeper water-supply zone that remains important for water uptake during key growth stages, especially from jointing to flowering. Before sampling, surface debris and stones were removed. Soil samples were then extracted using a soil auger, immediately sealed in aluminum boxes to minimize moisture evaporation, and transported to the laboratory. Fresh weight was measured using an electronic balance, after which the samples were dried in an oven at 105 °C for 8 h to determine dry weight. Soil moisture content was calculated using equation [22]:

$$SMC = \frac{w_2 - w_3}{w_3 - w_1} \times 100\% \quad (1)$$

where SMC denotes moisture content of soil mass (%), w_1 denotes mass of aluminum box (g), w_2 denotes mass of aluminum box with wet soil (g), w_3 denotes mass of aluminum box with dry soil (g).

2.2.3. UAV Data Preprocessing and Feature Extraction

In this study, Pix4Dmapper (version 4.5.6, Pix4D S.A., Prilly, Switzerland) software was used for the mosaicking and orthorectification of RGB and TIR images, and the TIR observations were converted into land surface temperature (Equation (2)). HS data were geometrically corrected using MegaCube (version 2.15.0, LICA United Technology Limited, Beijing, China) software, and radiometric calibration was performed based on radiometric calibration targets to generate reflectance cubes. All imagery was uniformly projected into the WGS84 UTM Zone 49N coordinate system. To achieve pixel-level fusion of multi-source

data, all data layers were resampled to a unified grid of 0.137 m to ensure spatial consistency and accuracy. For each GPS-located sampling point, a circular buffer with a radius of 0.4 m was generated in the UAV imagery, and the mean value of all pixels within the buffer was used as the representative feature value. This strategy helped mitigate the effects of canopy shadows, isolated abnormal pixels, and slight spatial mismatch between field sampling locations and image pixels.

$$LST = DN \times 0.04 - 273.15 \quad (2)$$

where LST represents land surface temperature (°C), and DN is the digital number value.

2.3. Methods

The input variables were categorized into seven modal configurations: single-modal (S1, S2, S3), dual-modal (S4, S5, S6), and tri-modal combination (S7) (Table 2). Subsequently, four automated machine learning algorithms—TPOT, AutoGluon, H2O AutoML, and FLAML—were employed to construct non-linear regression models between multi-modal features and measured SMC at soil layers of 0–20 cm and 20–40 cm.

Table 2. Summary of feature variables and data modalities under different input scenarios.

Scenario	Input Parameter	Features
S1	RGB	ME, VA, HO, CO, DS, EN, SM, COR
S2	HS	DI, RI, NDI, PI, M1~M6
S3	TIR	TVDI
S4	RGB + HS	ME, VA, HO, CO, DS, EN, SM, COR, M1~M6
S5	RGB + TIR	ME, VA, HO, CO, DS, EN, SM, COR, TVDI
S6	HS + TIR	DI, RI, NDI, PI, M1~M6, TVDI
S7	RGB + HS + TIR	ME, VA, HO, CO, DS, EN, SM, COR, DI, RI, NDI, PI, M1~M6, TVDI

2.3.1. Construction of RGB Indices

Based on the Gray Level Co-occurrence Matrix (GLCM) method, texture features were extracted from high-resolution UAV RGB images to characterize canopy spatial heterogeneity [23]. As shown in Figure 3, eight key texture indices were selected: Mean (ME), Variance (VA), Homogeneity (HO), Contrast (CO), Dissimilarity (DS), Entropy (EN), Second Moment (SM), and Correlation (COR). All feature extraction was performed using the ENVI (version 5.6, NV5 Geospatial Solutions, Inc., Superior, CO, USA) software platform. To ensure feature robustness, a 3 × 3 pixel sliding window was employed, and the average values of four directions (0°, 45°, 90°, and 135°) were calculated to eliminate directional dependency.

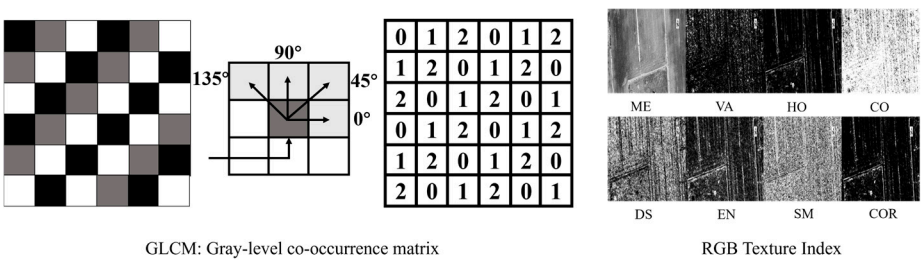


Figure 3. Extraction of wheat canopy texture information using the GLCM. The colored squares represent pixels with different gray levels, and the arrows indicate the directional relationships used for texture calculation.

2.3.2. Construction of Novel HS Indices

In this study, surface reflectance data were obtained using a UAV-mounted HS sensor covering the 400–1000 nm wavelength range with a total of 150 continuous spectral bands. Previous studies have demonstrated that spectral indices constructed from specific bands have potential for predicting SMC status [24–26]. However, the sensitivity of various spectral indices to soil moisture varies across crop types and ecological environments [27,28], which limits their applicability and generalization in practical scenarios. To systematically explore the hs features that are highly sensitive to soil moisture variations, this study constructed a series of novel spectral indices from both two-band and three-band combinations. Their effectiveness was quantitatively evaluated using statistical analysis methods. First, based on the 150 continuous spectral bands in the 400–1000 nm range, any two bands (B1, B2) were selected to construct four classical two-band spectral indices: Difference Index (DI), Ratio Index (RI), Normalized Difference Index (NDI), Perpendicular Index (PI) [16].

These two-band indices capture the relative spectral variation between different bands from various perspectives. Their mathematical expressions are as follows:

$$DI_{(B_i, B_j)} = B_i - B_j \tag{3}$$

$$RI_{(B_i, B_j)} = \frac{B_i}{B_j} \tag{4}$$

$$NDI_{(B_i, B_j)} = \frac{B_i - B_j}{B_i + B_j} \tag{5}$$

$$PI_{(B_i, B_j)} = \frac{B_i - 0.2703B_j - 0.1324}{\sqrt{1 + 0.2703^2}} \tag{6}$$

In the equations, B_i, B_j represent the spectral reflectance values at bands i and j, respectively, where $1 \leq i, j \leq 150$, and $i \neq j$. The constant term in the PI formula is derived based on the soil line parameters extracted from UAV spectral imagery (in this study, the soil line was obtained from pure soil pixels in the two-dimensional red-NIR spectral space, where red corresponds to B655 and NIR corresponds to B866. soil line: $y = 0.2703x + 0.1324$). The correlation and optimal indices between the bands were determined using Python (version 3.9) programming.

On this basis, a third band was further introduced to construct six novel three-band spectral indices, aiming to integrate more spectral information and thus improve the prediction accuracy and robustness of SMC. These indices encompass various mathematical forms such as ratios, normalization, differences, and squared sums, enabling the representation of more complex coupling mechanisms between spectral bands and offering stronger nonlinear fitting capabilities [29,30]. The specific mathematical expressions are as follows.

$$M_1 = B_1/B_2 \times B_3 \tag{7}$$

$$M_2 = B_1/(B_2 + B_3) \tag{8}$$

$$M_3 = (B_2 + B_3)/B_1 \tag{9}$$

$$M_4 = (B_1 - B_2)/((B_1 - B_2) - (B_1 - B_3)) \tag{10}$$

$$M_5 = (B_1 - B_2) - (B_1 - B_3) \tag{11}$$

$$M_6 = \left(B_1^2 + B_2^2 + B_3^2\right) \tag{12}$$

All possible combinations of spectral bands were exhaustively calculated, and the Pearson correlation coefficient (R) was used to evaluate the linear relationship between

each spectral index and the measured SMC. Among the four types of two-band indices (PI, DI, RI, and NDI) and the six types of three-band indices (M1–M6), the indices showing the strongest correlation with SMC in the 0–20 cm and 20–40 cm soil layers were selected as the optimal index forms and used as input variables for the prediction models. This provides a theoretical basis and variable support for constructing high-precision SMC inversion models.

2.3.3. Construction of Thermal Infrared Index

To further improve the accuracy and spatiotemporal adaptability of soil moisture monitoring, the temperature vegetation dryness index (TVDI) [31], which is constructed based on land surface temperature and the normalized difference vegetation index (NDVI), was introduced in this study to characterize the combined indication capability of land surface thermal conditions and vegetation cover for SMC (Figure 4) [32,33]. TVDI has been proven effective in describing the heat exchange processes and drought stress conditions among soil, vegetation, and atmosphere [34]. The calculation formula is as follows:

$$TVDI = \frac{Ts - T_{min}}{Ts_{max} - Ts_{min}} \quad (13)$$

$$Ts_{max} = a_{dry} + b_{dry} \times NDVI \quad (14)$$

$$Ts_{min} = a_{wet} + b_{wet} \times NDVI \quad (15)$$

where Ts_{min}, Ts_{max} indicate the minimum and maximum Ts values, respectively. a_{dry}, b_{dry}, a_{wet}, b_{wet} denote the intercepts and slopes of the dry and wet edges, respectively. The dry and wet edges were determined by linear fitting of the upper and lower boundaries in the Ts–NDVI feature space, yielding $T_{dry} = -62.49 \times NDVI + 74.84$ (R^2 = 0.78) and $T_{wet} = -28.21 \times NDVI + 33.59$ (R^2 = 0.55), respectively.

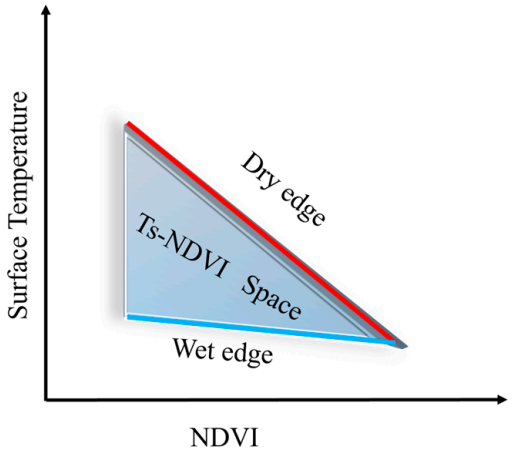


Figure 4. Schematic diagram of the TVDI (Ts-NDVI feature space).

2.3.4. Construction of Machine Learning Models

In this study, a systematic multi-modal data fusion framework was constructed to explore the retrieval performance of different data source combinations on soil moisture (Figure 5). Leveraging the advantages of AutoML in the automatic selection of candidate models and hyperparameter tuning, four advanced automated machine learning frameworks were selected: TPOT, AutoGluon, H2O AutoML, and FLAML.

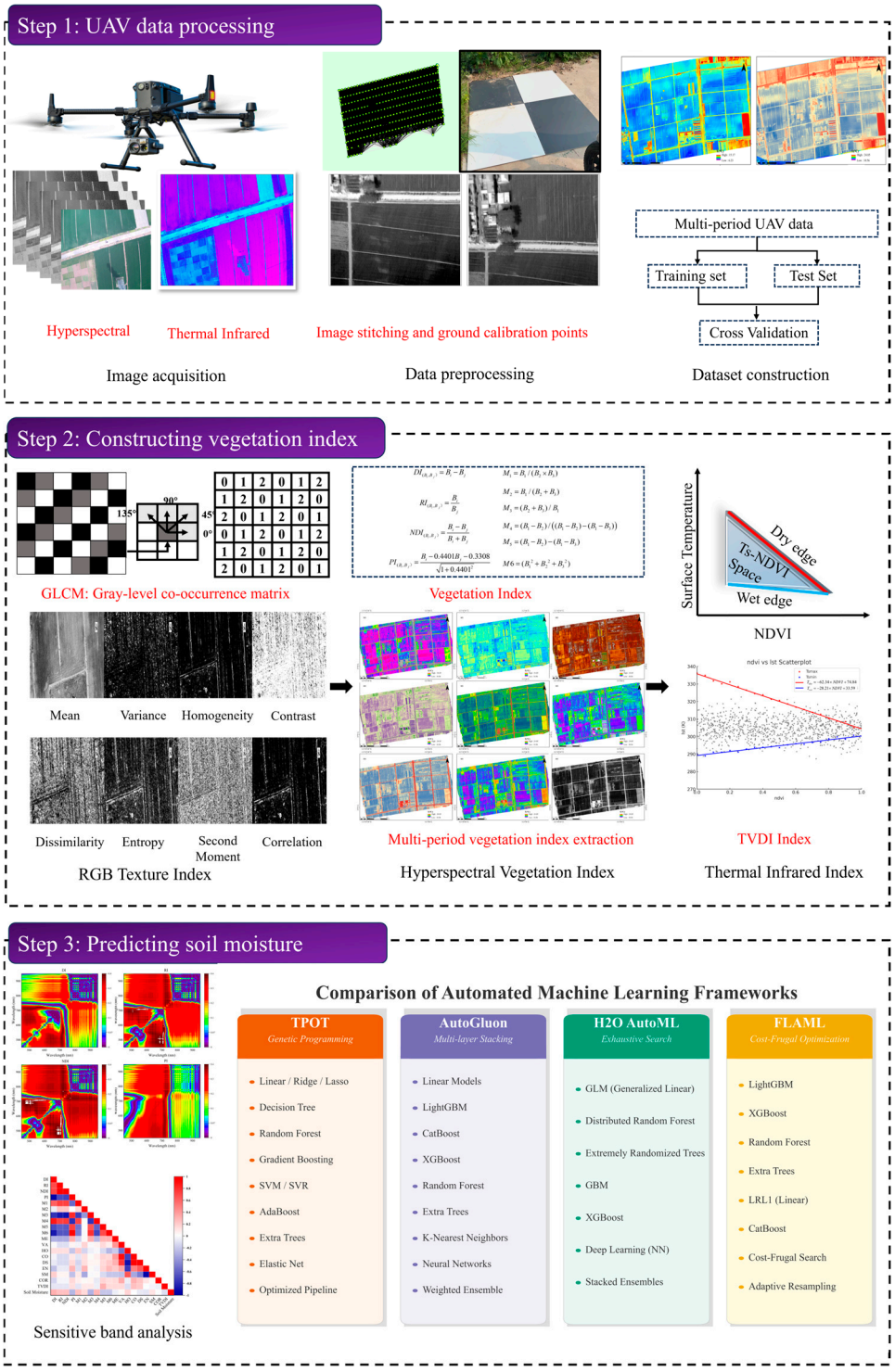


Figure 5. SMC prediction workflow based on multimodal UAV data and machine learning models.

TPOT: An evolutionary AutoML framework based on genetic programming [35]. By simulating the process of biological evolution, TPOT selects the machine learning pipelines with the highest fitness through multi-generational iteration. It can broadly search various algorithms, including Random Forest, XGBoost, and SVM, while simultaneously optimizing preprocessing steps, making it particularly adept at mining complex non-linear features in spectral data.

AutoGluon: This framework centers on a Multi-layer Stacking strategy and is designed for high-precision tasks [36]. Instead of relying on a single optimal model, AutoGluon

performs a weighted ensemble of predictions from various heterogeneous models, such as LightGBM, CatBoost, and Neural Networks. By combining k-fold bagging technology, it effectively utilizes the complementary strengths of different algorithms and performs exceptionally well in handling the heterogeneity of remote sensing data.

H2O AutoML: This framework focuses on the construction of Stacked Ensembles [37]. H2O automatically trains and validates various base models, including Generalized Linear Models (GLM), Distributed Random Forest (DRF), Gradient Boosting Machines (GBM), and Deep Learning (DL). Its core adopts the "Super Learner" strategy, optimizing the combined output of base models through a Metalearner, thereby balancing prediction accuracy and computational efficiency. To ensure reproducibility and manage computational resources, the maximum runtime (max_runtime_secs) for the H2O AutoML framework was explicitly set to 600 s (10 min) per fold during the cross-validation process, with an additional constraint of evaluating a maximum of 25 base models (max_models = 25).

FLAML: Renowned for its low latency and high computational efficiency [38], FLAML employs a Cost-Frugal Optimization (CFO) search strategy to iteratively select learners and hyperparameters that yield the best performance improvement per unit of computational cost. It supports high-performance estimators such as XGBoost, LightGBM, and Random Forest. Its lightweight design enables rapid convergence to the optimal model, making it highly suitable for modeling scenarios requiring rapid iteration.

The dataset used for modeling comprises 250 ground-truth SMC measurements collected during five independent flight missions between April and May 2024. A five-fold cross-validation method was adopted [3]. In each validation round, the dataset was randomly divided into five equal parts; four subsets were used sequentially for model training, while the remaining subset was used for validation. The final performance was evaluated based on the average values of the metrics from the five validation rounds to avoid overfitting and ensure model stability.

2.3.5. Model Evaluation Metrics

To comprehensively evaluate the prediction performance of different models in soil moisture estimation, three metrics were selected in this study: the Pearson correlation coefficient (R), root mean square error (RMSE), and relative root mean square error (rRMSE). Among them, the correlation coefficient R is used to measure the linear relationship between the predicted and observed values; RMSE reflects the absolute magnitude of the error between predictions and observations; and rRMSE standardizes the RMSE to indicate the relative proportion of the error in relation to the observed values. A higher R and lower RMSE and rRMSE indicate stronger model fitting ability and better prediction performance [39].

$$R = \frac{\sum_{i=1}^{n}(y_i - \overline{y_i})(\hat{y}_i - \overline{\hat{y}_i})}{\sqrt{\sum_{i=1}^{n}(y_i - \overline{y_i})^2} \times \sqrt{\sum_{i=1}^{n}(\hat{y}_i - \overline{\hat{y}_i})}} \quad (16)$$

$$RMSE = \sqrt{\frac{1}{n}\sum_{i=1}^{n}(y_i - \hat{y}_i)^2} \quad (17)$$

$$rRMSE = \frac{RMSE}{\overline{y}} \times 100\% \quad (18)$$

where y_i denotes the measured value of the i th sample, $\hat{y}_i$ denotes the predicted value of the i th sample, $\overline{y}$ denotes the mean of the measured value, $\overline{\hat{y}_i}$ denotes the mean of the predicted value, n denotes the number of samples.

2.4. Time-Independent Validation and Baseline Model Setup

2.4.1. Time-Independent Validation

To rigorously evaluate the model's temporal transferability and mitigate the risk of overfitting potentially caused by randomly mixing time-series data, this study adopts a Leave-One-Flight-Date-Out (LOFDO) cross-validation strategy. Unlike standard random five-fold cross-validation that ignores data acquisition time, the LOFDO scheme strictly separates the training and test sets based on five distinct UAV flight dates. In each iteration, data from four flight dates are used to train the model, while the data from the remaining flight date is entirely withheld as an independent test set. This process is repeated five times until each date has been used exactly once as the test set. The final performance is evaluated by calculating the average of the metrics across the five time-independent testing phases. This rigorous extrapolation scenario enables a more realistic assessment of the model's robustness when facing unseen phenological and meteorological conditions during the winter wheat growing season.

2.4.2. Traditional Machine Learning Baseline Models

To benchmark the performance of the AutoML frameworks and quantify their comparative advantages, three conventional machine learning algorithms widely adopted in agricultural remote sensing were constructed as baseline models: Random Forest (RF), Support Vector Regression (SVR), and Extreme Gradient Boosting (XGBoost). RF builds an ensemble of decision trees using bagging to reduce variance, while SVR and XGBoost are advanced gradient boosting frameworks known for handling complex tabular data efficiently with robust regularization techniques. The hyperparameters for these traditional baseline models were optimized using grid search coupled with cross-validation to ensure fair comparison. Their predictive performances under the optimal multi-modal data fusion scenario (S7) were subsequently compared against the best-performing AutoML model (H2O AutoML).

3. Results

3.1. Correlation Between SMC and Newly Constructed Two-Band and Three-Band Spectral Indices

Figure 6 illustrates the relationships between SMC and four newly developed two-band vegetation indices (DI, NDI, RI, and PI) at different soil depths. The R was used as an indicator to measure the correlation between spectral indices and SMC, and the detailed results are listed in Table 3. At the 0–20 cm soil layer, the red spectral region (688–706 nm) exhibited the highest correlation in all four types of two-band indices. Among them, the NDI showed the best performance, constructed using B566 and B693, with a correlation coefficient R as high as 0.616. The PI, composed of B554 and B706, had the lowest R value of 0.591. At the 20–40 cm depth, NDI still performed best, with the B566 and B693 combination achieving an R value of 0.569. The R values for DI, RI, and PI were 0.562, 0.564, and 0.559, respectively. The results in Figure 6 indicate that, in the 0–20 cm soil layer, the correlations of the two-band indices were significantly higher than those in the 20–40 cm layer, particularly showing a more sensitive response in the red spectral region. Ultimately, the combinations with the highest correlation to SMC at each depth from the four types of indices were selected as input variables for subsequent modeling.

Based on the above, further analysis was conducted on six newly developed three-band spectral indices. Table 4 lists the band combinations with the highest correlation to SMC. The results show that the R values of the new three-band indices were generally higher than those of the two-band indices. At the 0–20 cm depth, three indices achieved the highest R values within the visible light range, among which the combination B484/(B496 + B680) performed best, with an R value of 0.629. For the 20–40 cm depth, the combination of blue

and red bands, B546/(B693 + B706), achieved the highest R value of 0.590. In addition, the maximum R values of the other five indices across the visible and near-infrared spectral regions were 0.580, 0.577, 0.588, 0.586 and 0.540, respectively. The results indicate that the inclusion of infrared bands enhances the sensitivity of the indices to SMC variation, and the constructed spectral indices are able to effectively reflect field SMC dynamics. All of these indices are based on combinations of three bands within the visible and near-infrared regions and demonstrated reliable correlations with SMC (R > 0.540), effectively capturing the key characteristics of SMC variability.

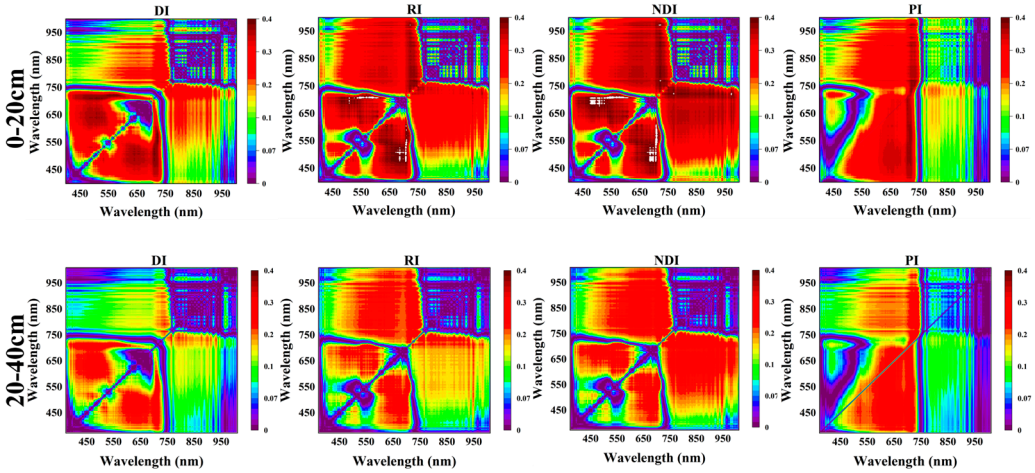


Figure 6. R^2 distribution of two-band spectral indices for SMC at 0–20 cm and 20–40 cm soil depths.

Table 3. Correlation between novel dual-band spectral indices and soil moisture content.

Index	Depth	Spectral Index	|R|
DI	0–20 cm	B554 − B706	0.602
RI		B587/B688	0.613
NDI		(B578 − B688)/(B578 + B688)	0.616
PI		$B706 - 0.2703 \times B554 - 0.1324/(\sqrt{1 + 0.2703^2})$	0.591
DI	20–40 cm	B554 − B706	0.562
RI		B578/B688	0.560
NDI		(B578 − B688)/(B578 + B688)	0.569
PI		$B706 - 0.2703 \times B554 - 0.1324/(\sqrt{1 + 0.2703^2})$	0.559

Note: B denotes the spectral band and the number denotes the spectral wavelength.

Table 4. Correlation between the novel three-band spectral index and SMC.

Index	Depth	Spectral Index	|R|
M1	0–20 cm	B546/(B689 × B731)	0.605
M2		B484/(B496 + B680)	0.629
M3		(B496 + B688)/B484	0.623
M4		(B566 − B591)/((B566 − B591) − (B566 − B706))	0.620
M5		(B431 − B484) − (B431 − B693)	0.617
M6		$(B406^2 + B410^2 + B705^2)$	0.562
M1	20–40 cm	B566/(B667 × B727)	0.580
M2		B546/(B693 + B706)	0.590
M3		(B545 + B616)/B706	0.577
M4		(B566 − B616)/((B566 − B616) − (B566 − B701))	0.588
M5		(B423 − B467) − (B423 − B608)	0.586
M6		$(B406^2 + B410^2 + B705^2)$	0.540

Note: B denotes the spectral band and the number denotes the spectral wavelength.

In comparison, by introducing an additional spectral dimension, three-band indices capture the spectral characteristics of soil moisture more comprehensively than dual-band indices, and the retrieval performance for the 0–20 cm depth was superior to that for the 20–40 cm depth.

Figure 7 displays the correlation coefficient matrices between spectral indices, texture features, and TIR indices and SMC across five observation dates. The color intensity of the heatmaps intuitively reflects the temporal dynamic changes in the response intensity of each variable to SMC. In terms of the time series, the color contrast in the correlation coefficient matrices for 22 April and 17 May was the strongest, indicating that the HS-constructed vegetation indices and RGB texture indices maintained high levels of correlation with SMC. In contrast, the overall correlations on 17 April and 10 May were relatively weak, suggesting that the correlation between SMC and remote sensing features exhibits significant temporal heterogeneity. This fluctuation may be related to changes in crop coverage and the soil surface status following irrigation or rainfall.

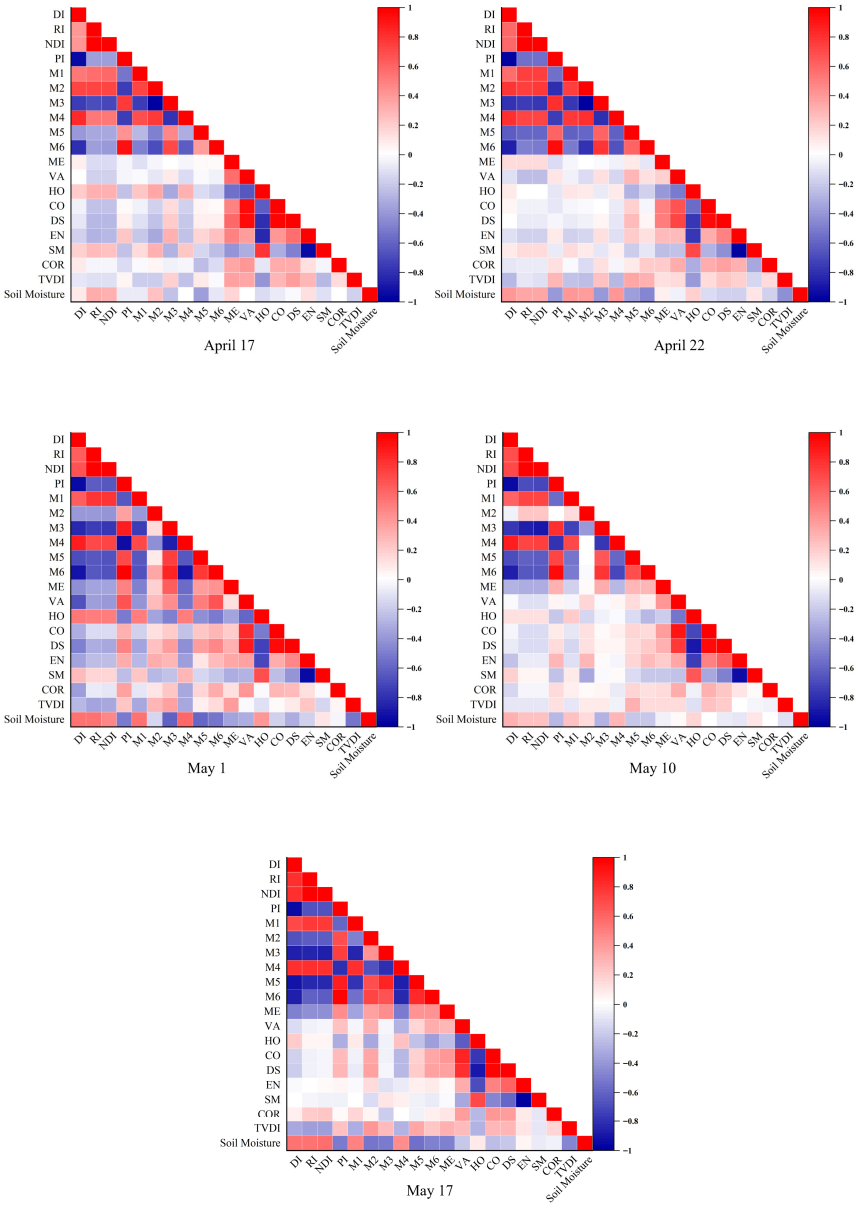


Figure 7. Correlation analysis between vegetation indices and SMC on five observation dates based on multimodal UAV remote sensing.

Regarding the response patterns of multiple indices, the dual-band indices consistently maintained a significant positive correlation with SMC, demonstrating strong temporal robustness. The three-band indices M3 and M6 showed a significant negative correlation with SMC; this response direction, opposite to that of the dual-band indices, indicates that the three-band indices captured non-linear complementary information regarding the spectral response of soil moisture. The TIR index TVDI maintained a consistent negative correlation across all periods, validating the physical negative feedback mechanism between land surface temperature and soil moisture. Overall, despite fluctuations in correlation for single phases, the novel dual-band and three-band indices constructed in this study were able to maintain strong sensitivity across multiple phases. They provided positive and negative feature dimensions, respectively, and when combined with texture and temperature information, provided a reliable and diverse variable basis for the subsequent construction of high-precision soil moisture retrieval models.

3.2. SMC Prediction Based on Machine Learning

To investigate the potential of multi-source remote sensing data in soil moisture monitoring, this study designed seven input modal combinations (S1–S7) and comparatively evaluated the regression performance of four automated machine learning frameworks: AutoGluon, FLAML, H2O AutoML, and TPOT (Table 5). Among the four AutoML frameworks, H2O AutoML demonstrated the best generalization ability and robustness. Across most sensor combinations and both soil depths, the evaluation metrics of H2O AutoML were superior to those of the other three algorithms. Taking the S7 combination as an example, in the 0–20 cm soil layer, the R of H2O AutoML reached 0.77, and the RMSE was 1.99%, outperforming FLAML (R = 0.71), AutoGluon (R = 0.70), and TPOT (R = 0.69). This result indicates that H2O AutoML can more effectively capture non-linear features within high-dimensional multi-source heterogeneous data, achieving higher retrieval accuracy under limited sample conditions.

Table 5. SMC statistics for different machine learning algorithms to validate 0–20 cm and 20–40 cm soil depths.

Sensor Type	Metrics	AutoGluon		FLAML		H2O AutoML		TPOT	
		20 cm	40 cm	20 cm	40 cm	20 cm	40 cm	20 cm	40 cm
S1	R	0.25	0.30	0.28	0.27	0.43	0.45	0.09	0.28
	RMSE (%)	3.12	3.16	3.09	3.20	2.92	2.96	3.28	3.20
	rRMSE (%)	21.5	24.8	21.3	25.1	20.0	23.2	22.6	25.1
S2	R	0.64	0.59	0.65	0.56	0.72	0.66	0.62	0.57
	RMSE (%)	2.47	2.68	2.46	2.73	2.21	2.48	2.54	2.71
	rRMSE (%)	17.0	21.0	16.9	21.4	15.1	19.5	17.5	21.2
S3	R	0.47	0.42	0.60	0.55	0.64	0.64	0.61	0.53
	RMSE (%)	2.85	3.04	2.58	2.75	2.47	2.56	2.56	2.82
	rRMSE (%)	19.6	23.8	17.7	21.6	16.9	20.1	17.6	22.1
S4	R	0.64	0.59	0.65	0.60	0.72	0.68	0.63	0.64
	RMSE (%)	2.47	2.68	2.46	2.66	2.22	2.44	2.51	2.55
	rRMSE (%)	17.0	20.9	16.9	20.8	15.2	19.1	17.3	20.0
S5	R	0.55	0.50	0.58	0.53	0.65	0.64	0.58	0.52
	RMSE (%)	2.69	2.88	2.62	2.82	2.44	2.57	2.64	2.85
	rRMSE (%)	18.5	22.6	18.0	22.1	16.8	20.2	18.1	22.3
S6	R	0.69	0.63	0.69	0.65	0.76	0.72	0.72	0.62
	RMSE (%)	2.34	2.57	2.33	2.52	2.10	2.29	2.23	2.60
	rRMSE (%)	16.1	20.2	16.0	19.8	14.5	17.9	15.3	20.4
S7	R	0.70	0.66	0.71	0.63	0.77	0.72	0.69	0.61
	RMSE (%)	2.23	2.36	2.18	2.45	1.99	2.17	2.27	2.48
	rRMSE (%)	15.4	18.3	15.1	18.9	13.6	16.7	15.7	19.2

Figures 8 and 9 visually display the scatter distribution characteristics of the SMC values predicted by the H2O AutoML model against the measured values for soil depths of 0–20 cm and 20–40 cm under different input modalities. Overall, most sample points are closely clustered around the 1:1 standard line, confirming the excellent fitting capability of the H2O AutoML model in non-linear regression tasks. In terms of vertical depth comparison, the model's prediction accuracy for the 0–20 cm surface soil layer (R = 0.77) was generally superior to that for the 20–40 cm deep soil layer (R = 0.72). As the input variables expanded from single-modal to multi-modal, the scatter distribution showed a significant trend of convergence towards the 1:1 line, with outliers significantly reduced. In particular, the combination scheme fusing HS, RGB, and TIR data showed high consistency between predicted and measured values, indicating that the synergistic effect of multi-source data effectively enhanced the representation capability of the feature space. This fully validates the strong generalization ability and robustness of the H2O AutoML model when processing high-dimensional complex features.

Figure 10 further compares the prediction performance metrics of the four AutoML algorithms under different modal combinations from a quantitative perspective. Overall, the combined use of multi-sensor data significantly improved SMC estimation accuracy compared to single sensors, with H2O AutoML maintaining the best performance across most combinations. The synergistic effect between TIR and HS data was significant. Taking the 0–20 cm depth (Figure 10a) as an example, when using the H2O AutoML algorithm, the S6 combination (fusing TIR and HS) achieved an R of approximately 0.76, which was superior to the results of using HS alone (S2, R = 0.72) and TIR alone (S3, R = 0.64). This indicates that the land surface temperature information provided by the TIR bands can effectively supplement the limitations of spectral reflectance in moisture retrieval, significantly reducing prediction error. The marginal effect of RGB data presented a polarized trend. In the H2O AutoML and FLAML algorithms, the S7 combination achieved only a minor accuracy improvement compared to S6 ($R < 0.02$). This suggests that compared to HS and TIR bands, which are rich in physical meaning, broadband RGB imagery is prone to causing feature redundancy and overfitting issues in retrieval models, and its effectiveness as an auxiliary variable depends on the robustness of the algorithm to noise.

Figure 11 further quantifies the distribution range of the predictive performance of the algorithms. In terms of algorithm stability, H2O AutoML exhibited the narrowest error distribution range and the fewest outliers in terms of R and RMSE metrics (Figure 11a,c), indicating its superior robustness as the optimal model when dealing with complex multi-source heterogeneous data. Regarding the vertical spatial distribution, model accuracy exhibited a distinct depth dependency. At the 0–20 cm soil depth, the R value range of the SMC estimates was between 0.45 and 0.72, with a mean of 0.64, whereas at the 20–40 cm depth, the fluctuation range of R values expanded to 0.32–0.68, with a mean of 0.57. This vertical attenuation of accuracy suggests that while multi-source fusion algorithms can retrieve deep soil moisture via indirect correlations, prediction uncertainty accumulates with increasing depth, making the reliability of surface SMC retrieval superior to that of the deep layer.

To reveal the internal decision-making mechanism of the automated machine learning models, the SHAP method was introduced to quantitatively analyze the contribution of input features. The ranking of the mean absolute SHAP values of features for the four AutoML algorithms at 0–20 cm and 20–40 cm soil depths (Figure 12) intuitively reflects the marginal contribution of each variable to the SMC prediction results. Regardless of the algorithm or soil depth, the TVDI consistently ranked first in feature importance, indicating that land surface temperature is the most critical factor for retrieving soil moisture. In terms of physical mechanism, TVDI integrates complementary information of LST and Vegetation

Index (VI), directly reflecting the intensity of surface evapotranspiration and changes in crop latent heat flux, thereby establishing the most direct physical link with soil moisture.

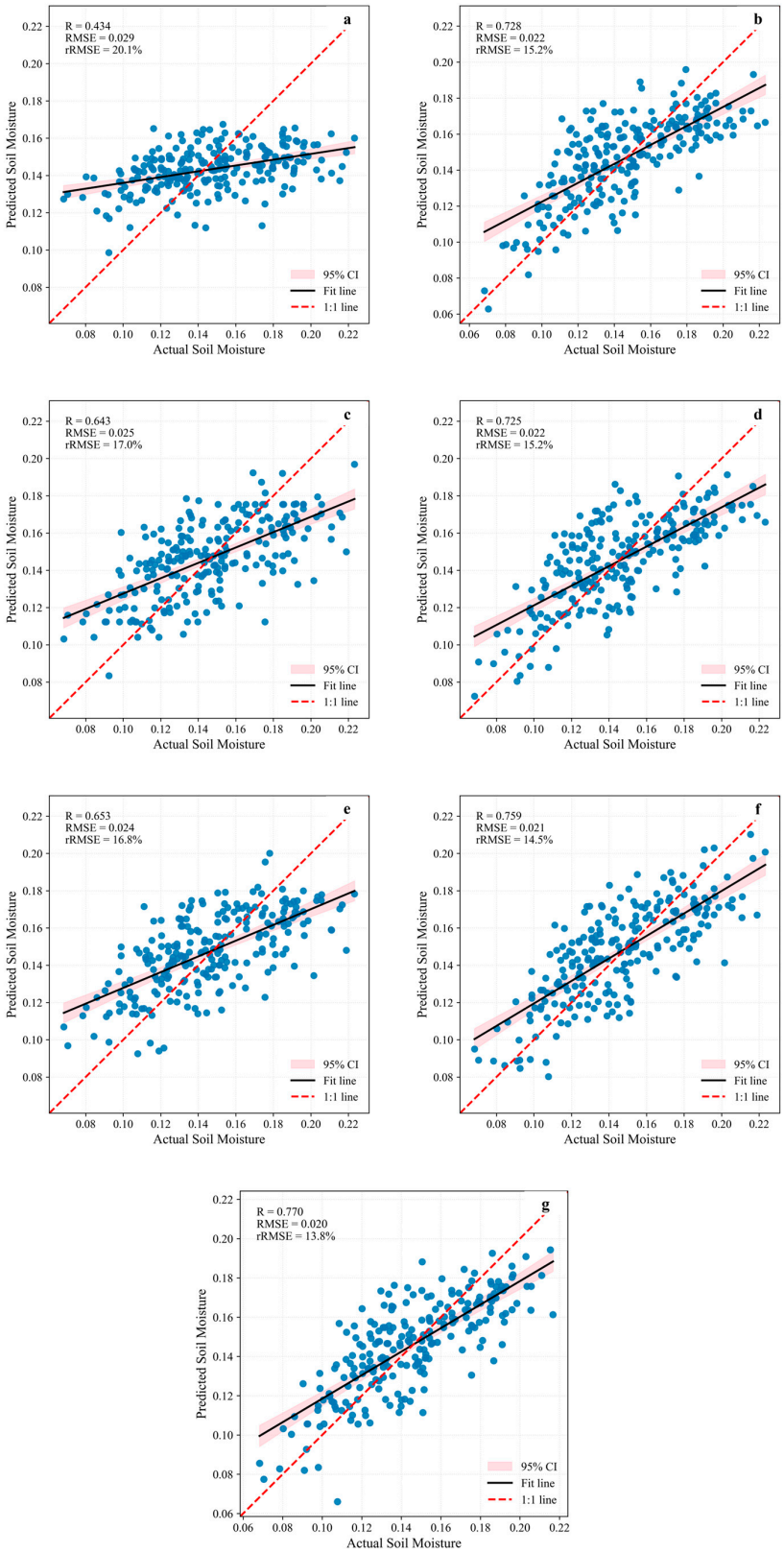


Figure 8. Retrieval results of SMC at 0–20 cm depth based on the H2O AutoML algorithm and different sensor combinations. (**a**–**g**) correspond to combinations S1–S7, respectively. The blue dots represent individual samples.

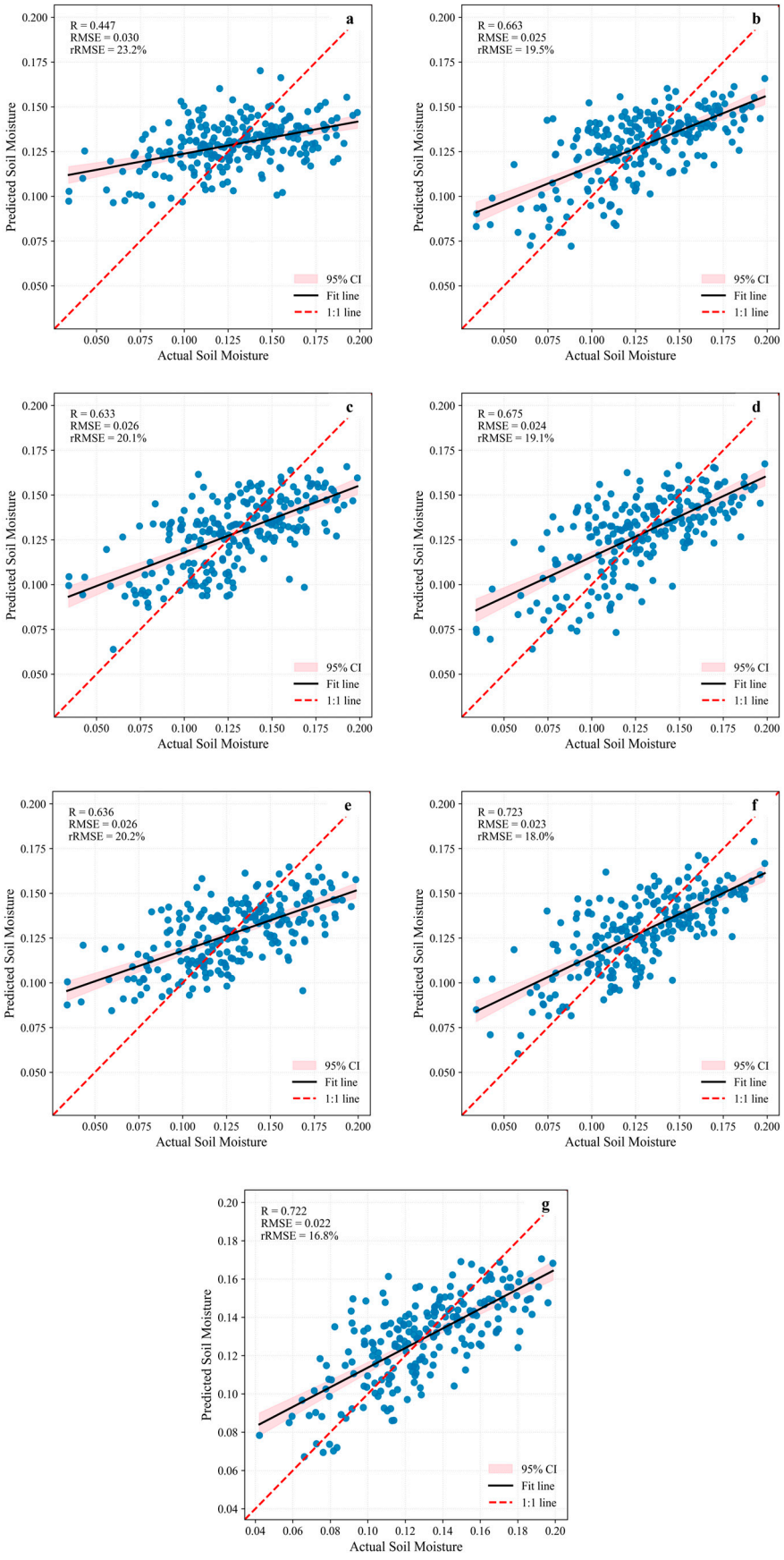


Figure 9. Retrieval results of SMC at 20–40 cm depth based on the H2O AutoML algorithm and different sensor combinations. (**a**–**g**) correspond to combinations S1–S7, respectively. The blue dots represent individual samples.

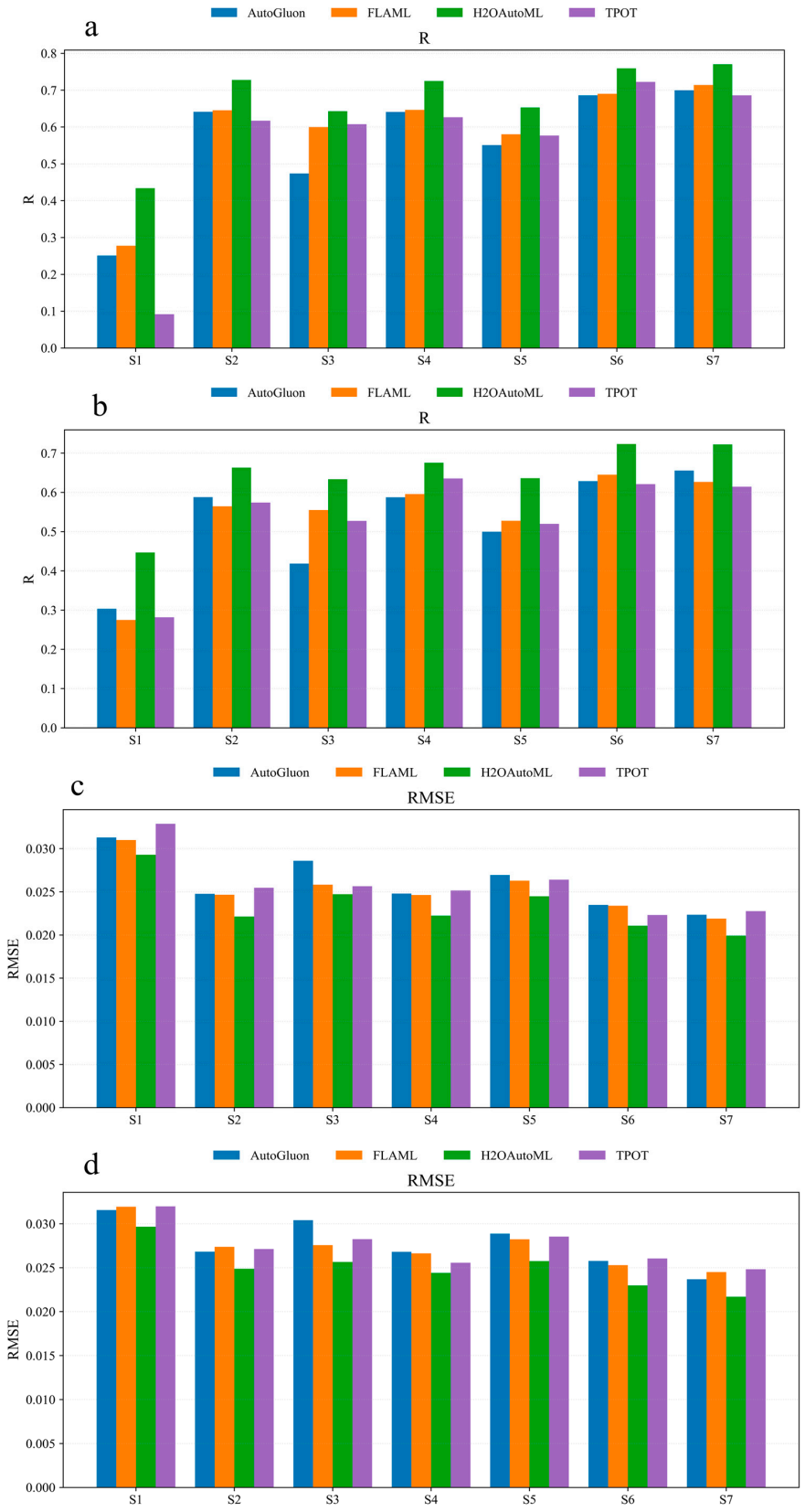


Figure 10. *Cont*.

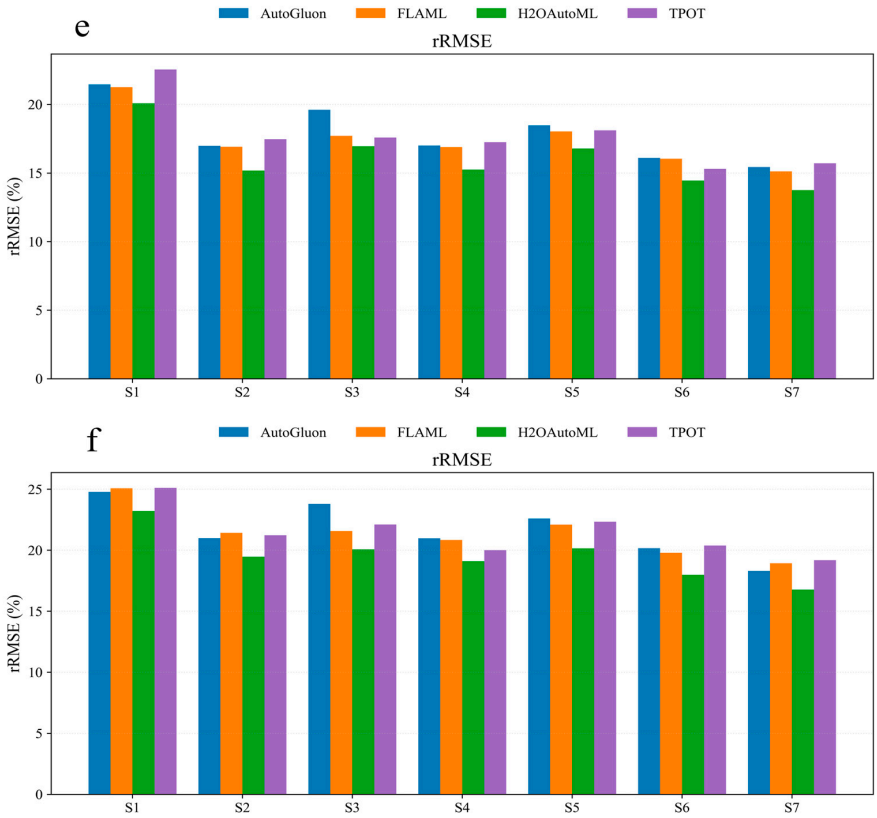


Figure 10. Comparison of accuracy evaluation metrics for SMC estimation using different algorithms and modal data combinations. (**a**,**c**,**e**) R, RMSE, and rRMSE of SMC at 0–20 cm depth; (**b**,**d**,**f**) R, RMSE, and rRMSE of SMC at 20–40 cm depth.

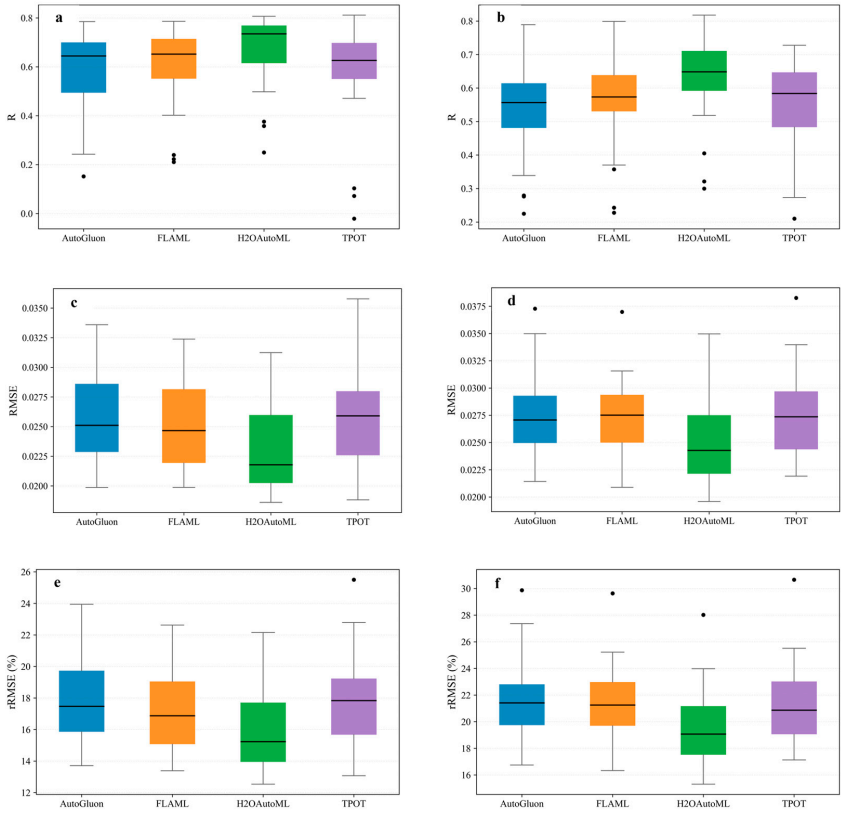


Figure 11. Box plots showing the distribution of R, RMSE, and rRMSE for SMC estimation by different algorithms based on multi-modal data. (**a**,**c**,**e**) 0–20 cm; (**b**,**d**,**f**) 20–40 cm. The black dots represent outliers.

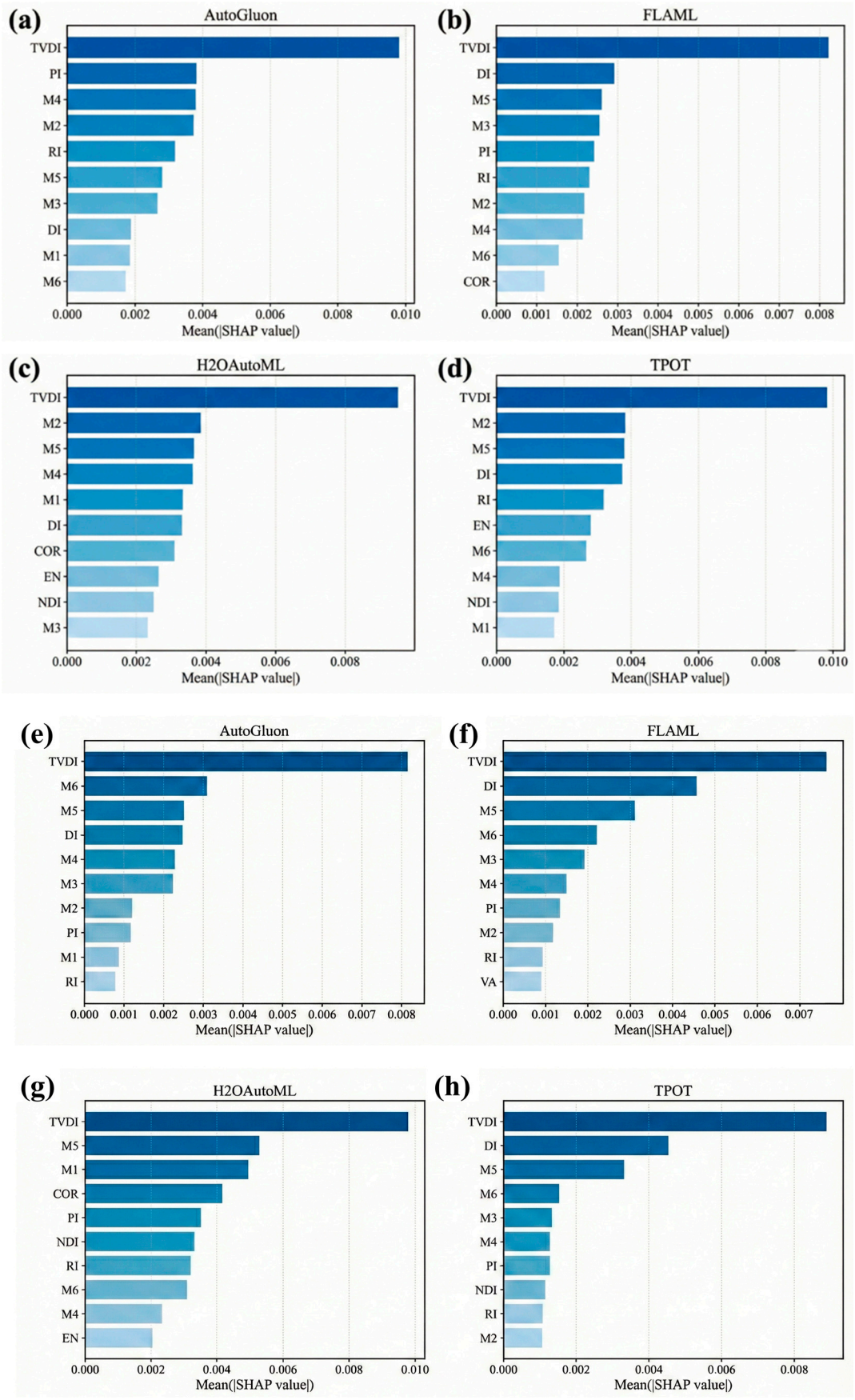


Figure 12. Mean (|SHAP value|) of important features for different AutoML models. (**a**) AutoGluon, 0–20 cm; (**b**) FLAML, 0–20 cm; (**c**) H2O AutoML, 0–20 cm; (**d**) TPOT, 0–20 cm; (**e**) AutoGluon, 20–40 cm; (**f**) FLAML, 20–40 cm; (**g**) H2O AutoML, 20–40 cm; (**h**) TPOT, 20–40 cm.

Regarding the constructed novel three-band indices, in the H2O AutoML model at the 0–20 cm depth, the SHAP values of M2 and M5 were second only to TVDI and significantly higher than those of traditional dual-band indices. This indicates that by introducing an additional spectral dimension, the three-band indices successfully captured the non-linear moisture signals in the mixed spectra of soil and vegetation, serving as important supplementary variables second only to TIR features. In contrast, texture features derived from RGB images ranked relatively low in most models. This suggests that within the high-dimensional feature space containing HS and TIR data, the texture information provided by broadband RGB exhibits significant redundancy, and its contribution to model accuracy is relatively limited.

Building on the global feature importance analysis, a SHAP summary plot (Figure 13a) was generated for the 0–20 cm soil layer to visualize the distribution of feature effects across all samples. Consistent with the mean absolute SHAP rankings, TVDI was the most influential variable; higher TVDI values (indicating elevated surface water stress) consistently corresponded to negative SHAP values, driving down the predicted SMC. The summary plot also confirmed the critical roles of DI, M5, and PI, demonstrating that these diverse spectral indices provide highly sensitive, complementary information for shallow soil moisture retrieval.

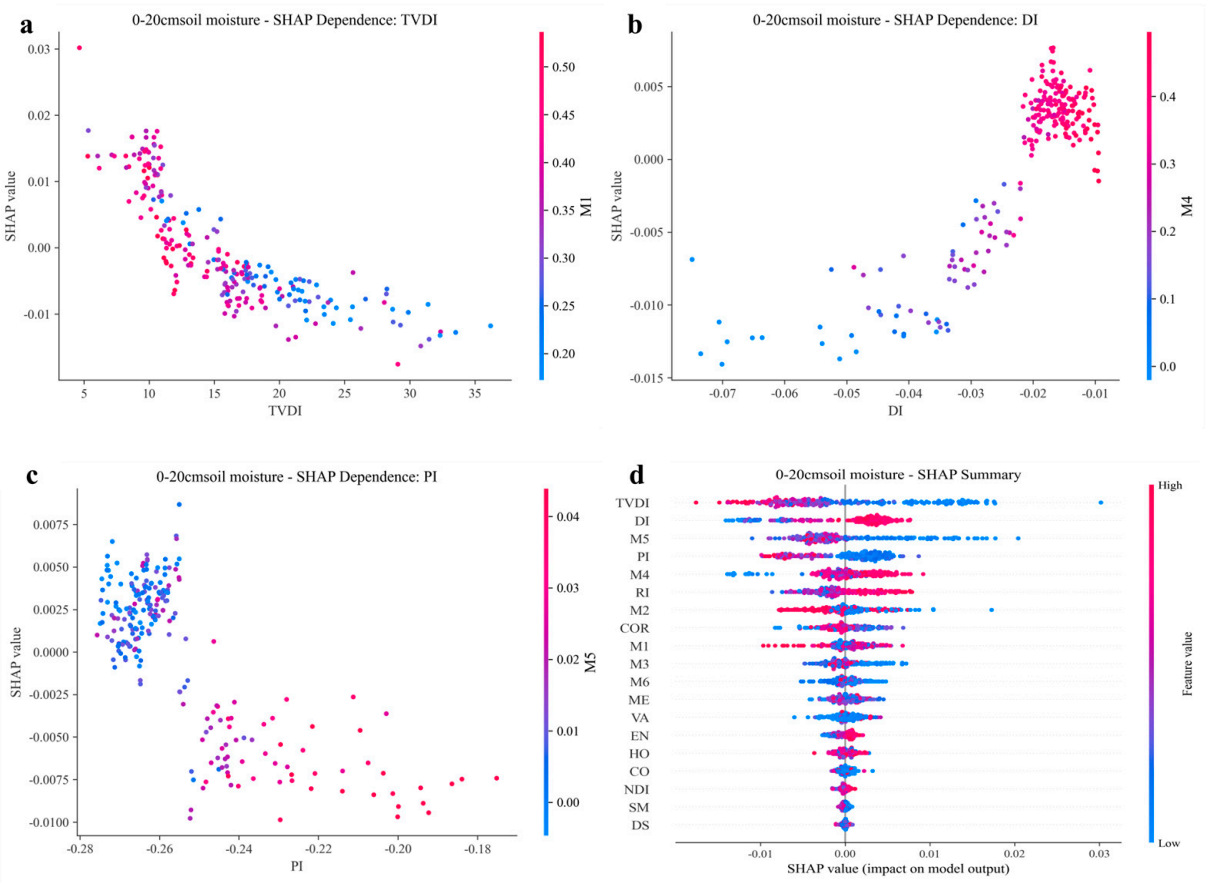


Figure 13. SHAP-based interpretation results for 0–20 cm soil moisture prediction. (**a**) SHAP dependence plot of TVDI; (**b**) SHAP dependence plot of DI; (**c**) SHAP dependence plot of PI; and (**d**) SHAP summary plot.

To further elucidate these complex dynamics, SHAP dependence plots were generated for TVDI, DI, and PI (Figure 13a–c) to reveal their nonlinear effects on the model output. The TVDI plot showed a strong negative trend with an apparent biophysical saturation effect under severe stress conditions. The hyperspectral indices exhibited distinct threshold-like

patterns: DI demonstrated a nonlinear functional leap with its positive contribution sharply increasing near −0.03, while PI displayed an abrupt shift from a positive to a negative impact when exceeding approximately −0.25. Furthermore, the color-coded dispersions within these plots suggested strong interaction effects among the features. These insights confirm that shallow soil moisture prediction within the H2O AutoML framework is successfully driven by nonlinear feature responses and coupled multi-variable mechanisms, rather than simple linear correlations.

3.3. Time-Independent Validation Results and Comparison with Traditional Models

Figure 14 illustrates the predictive performance of the optimal H2O AutoML model under the rigorous LOFDO cross-validation scheme within the fully fused multimodal data scenario (S7). Compared to random data partitioning, the model's transition to a temporal extrapolation scenario resulted in an expected slight decrease in prediction accuracy. Specifically, at the 0–20 cm depth (Figure 14a), the model's R-value decreased from 0.77 under random validation to 0.682, the RMSE was 0.024, and the rRMSE increased from 13.8% to 16.19%. At the 20–40 cm depth (Figure 14b), the R-value dropped from 0.72 to 0.629, the RMSE was 0.026, and the rRMSE increased from 16.8% to 20.13%. This performance difference is primarily attributed to the significant temporal heterogeneity exhibited by the canopy structure and surface thermal environment across different growth stages of winter wheat. Conventional random cross-validation allows the model to perform interpolation within a known global data distribution, whereas the LOFDO scheme forces the model to conduct more challenging extrapolation predictions under completely unseen temporal scenarios. Despite facing such stringent testing conditions, the H2O AutoML model still maintained relatively stable and reliable inversion performance under the LOFDO validation. This fully demonstrates that the multi-source fusion framework constructed in this study indicates that the proposed multimodal framework has improved temporal transferability within the study area and growing season, rather than simply memorizing date-specific patterns.

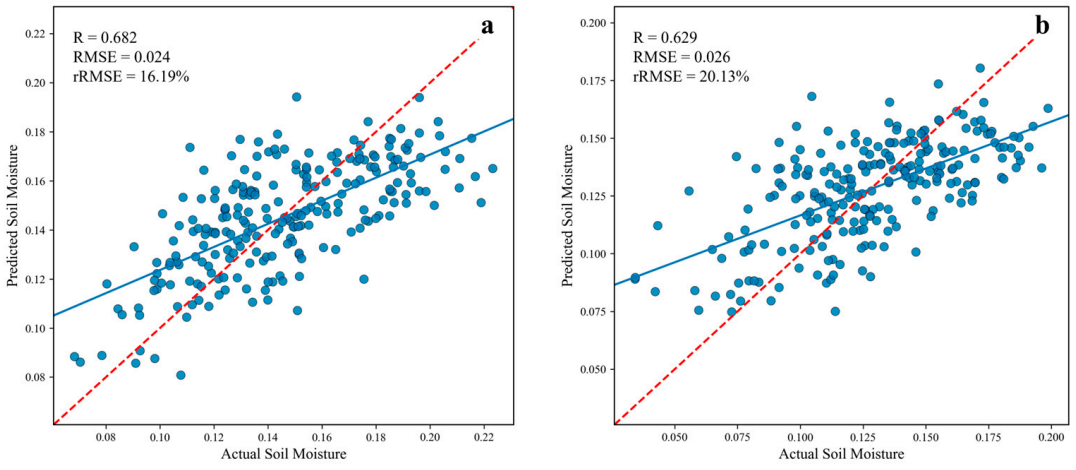


Figure 14. Soil moisture inversion accuracy assessment of the H2O AutoML model based on LOFDO cross-validation. The blue dots represent individual samples, the blue solid line represents the fitted regression line, and the red dashed line indicates the 1:1 line. (**a**) 0–20 cm depth; (**b**) 20–40 cm depth.

Under the rigorous LOFDO evaluation framework, we further compared the predictive accuracy of the H2O AutoML model with traditional machine learning baseline models (RF, SVR, and CatBoost), as detailed in Table 6.

Table 6. Comparison of soil moisture predictive performance between H2O AutoML and traditional baseline models under rigorous LOFDO cross-validation.

Depth	Model	R	RMSE	rRMSE (%)
0–20 cm	H2O AutoML	0.682	0.024	16.19
	RF	0.618	0.026	17.64
	SVR	0.621	0.026	17.54
	XGBoost	0.584	0.027	18.47
20–40 cm	H2O AutoML	0.629	0.026	20.13
	RF	0.595	0.027	20.97
	SVR	0.570	0.027	21.48
	XGBoost	0.570	0.028	21.79

The results indicate that the H2O AutoML model consistently and significantly outperforms traditional single-architecture models in terms of temporal generalization capability. Specifically, the average R-values achieved by RF, SVR, and XGBoost were 0.606, 0.595, and 0.577, respectively, all of which are notably lower than the 0.655 achieved by H2O AutoML. The superior performance of the H2O framework in this stringent, time-independent validation is primarily attributed to its built-in stacked ensemble meta-learning strategy. By dynamically weighting and fusing the predictive advantages of diverse base learners, H2O AutoML effectively mitigates the high variance and extrapolation bias issues that single tree-based models or kernel methods typically encounter when faced with time-shifted multimodal data distributions.

3.4. Spatial Distribution of Soil Moisture Content

Figure 15 presents the spatial distribution maps of regional SMC predicted by the H2O AutoML model based on the fusion of HS, TIR, and RGB multi-source data. The results show that this method effectively distinguishes between different surface types, such as roads, vegetation-covered farmland, and bare soil, reflecting the spatial heterogeneity of soil moisture at the regional scale. The spatial distribution patterns of SMC at different depths were generally consistent, both exhibiting clear spatial structures and gradient variations. For example, between 17 April and 17 May, the average SMC in the 0–20 cm soil layer decreased by approximately 0.4%, while the SMC in the 20–40 cm layer decreased by about 0.3%. Overall, soil moisture content at both depths showed a gradual decline over time, indicating a typical pattern of spatiotemporal synchrony. This phenomenon is mainly influenced by rising temperatures and increased evapotranspiration, which lead to continuous loss of soil moisture. These results validate the effectiveness and applicability of multi-source remote sensing fusion combined with machine learning in monitoring soil moisture dynamics at the regional scale. It demonstrates that the H2O AutoML model, based on the fusion of RGB, TIR, and HS data, can effectively predict the spatiotemporal distribution of SMC and provide a scientific basis for precision irrigation management at the regional level.

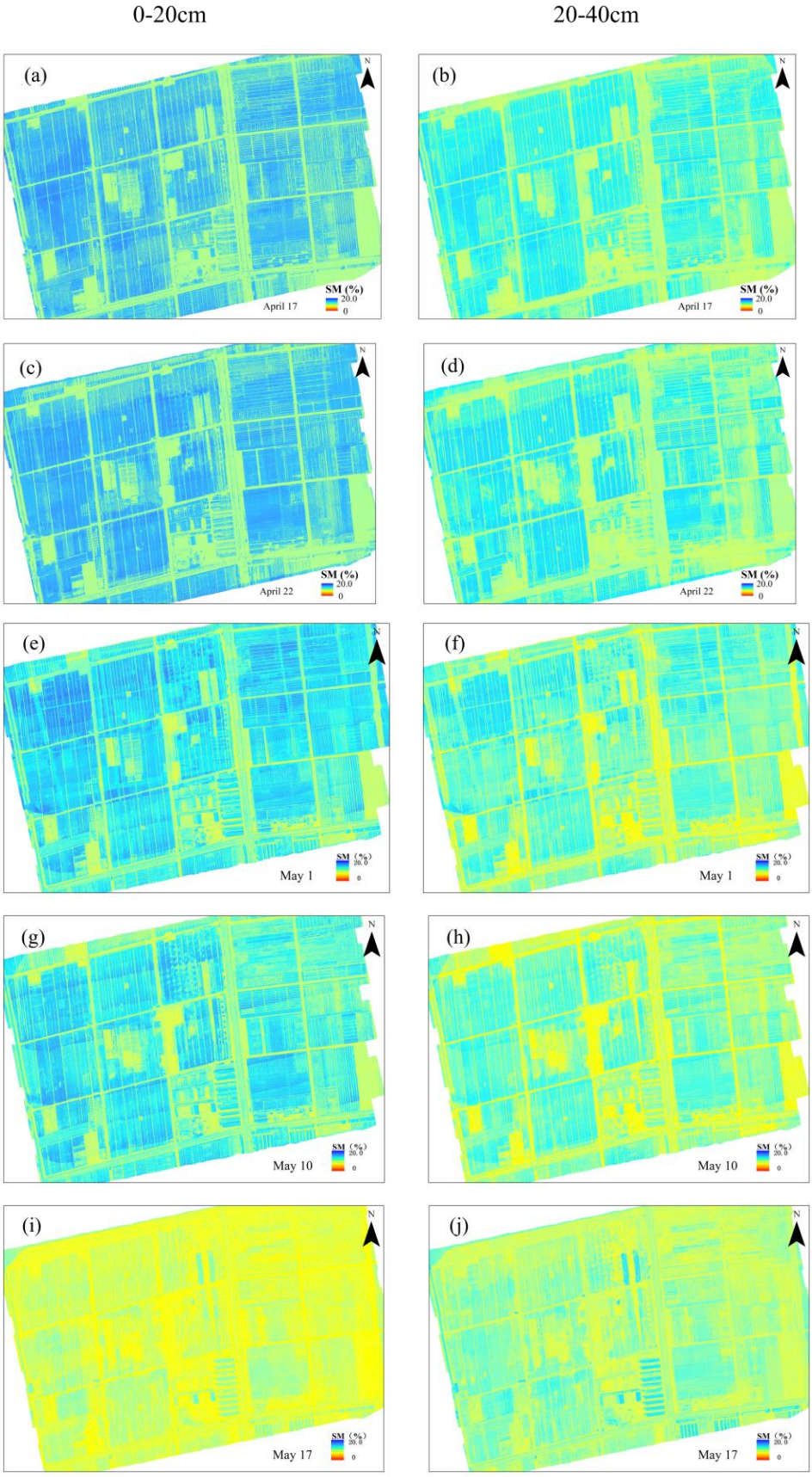


Figure 15. Predicted SMC using the H2O AutoML regression model based on UAV HS, TIR and RGB data. (**a**) April 17, 0–20 cm; (**b**) April 17, 20–40 cm; (**c**) April 22, 0–20 cm; (**d**) April 22, 20–40 cm; (**e**) May 1, 0–20 cm; (**f**) May 1, 20–40 cm; (**g**) May 10, 0–20 cm; (**h**) May 10, 20–40 cm; (**i**) May 17, 0–20 cm; (**j**) May 17, 20–40 cm.

4. Discussion

4.1. Performance of UAV-Based Multimodal Data in SMC Prediction

In this study, high-accuracy estimation of regional-scale SMC was achieved during the key growth stages of winter wheat using UAV-based multi-source remote sensing data. In contrast to previous studies that primarily relied on multispectral and TIR data, this research integrated RGB, HS, and TIR sensor data mounted on UAVs. It systematically explored spectral response characteristics within the 400–1000 nm range, developed novel two-band and three-band vegetation indices, and performed multi-source data fusion analysis incorporating RGB and TIR temperature features. Based on this foundation, multiple machine learning algorithms were employed to comprehensively evaluate the performance of different models in predicting SMC during critical wheat growth periods, ultimately constructing an optimal prediction model with high accuracy and strong generalization capability. Different types of sensors provide distinct and complementary dimensions of information acquisition and feature contributions. RGB cameras capture vegetation texture and color information, which aids in revealing canopy structure changes [3]. TIR sensors capture canopy and surface temperatures, indirectly reflecting crop water stress and SMC conditions [40]. Meanwhile, HS sensors, with their continuous and narrow-band spectral coverage, are capable of capturing fine spectral responses of the canopy under different water conditions, making it possible to precisely identify water-sensitive spectral bands.

Compared with multispectral data, HS data have significant advantages in the number of bands and spectral resolution, allowing for more accurate extraction of spectral features related to SMC, especially under vegetative cover. Furthermore, the combined use of multi-sensor data provides a more comprehensive set of input features for modeling, significantly enhancing the predictive accuracy and robustness of various machine learning models. This finding validates previous conclusions regarding the potential of multi-source remote sensing fusion for SMC estimation [13,41]. More importantly, studies published in the past two years have further confirmed that multimodal fusion is a pivotal direction in UAV-based soil moisture monitoring. For example, Yu et al. reported that integrating UAV and Sentinel-1/2 observations improved winter wheat soil moisture estimation across scales, with plot-scale R^2 values reaching 0.775 and 0.723 for the 0–20 cm and 20–40 cm layers, respectively [42]. Likewise, Vahidi et al. demonstrated that combining RGB-thermal imagery with subsurface information improved soil moisture prediction at both shallow and deeper layers, highlighting the indispensable role of thewrmal information [43]. A recent winter wheat study also showed that fusing RGB, multispectral, and TIR data consistently outperformed single-source inputs, with ensemble learning achieving the highest overall accuracy [44]. These studies, alongside our present results, emphasize that multimodal fusion not only improves prediction accuracy but also effectively mitigates the limitations of individual sensors under dense canopy cover.

Features such as vegetation texture, canopy temperature, and HS reflectance are all indispensable in SMC modeling, and their integration is crucial for reliable regional-scale dynamic monitoring. The combined use of HS and TIR data demonstrated particularly significant advantages, effectively overcoming the gradual saturation issue commonly associated with standalone optical bands [19]. However, when RGB data were integrated with HS and TIR data, the model accuracy improvement in the H2O AutoML and FLAML algorithms was marginal. This may be attributed to the overlap between HS and RGB bands, which induces data redundancy and subsequently affects model performance [40]. Related studies have also confirmed that significant spectral overlap exists between RGB bands and the visible region of HS data, and such redundant features may reduce the predictive capability of the models [16,45]. Therefore, in practical applications, data combinations must be selected carefully to avoid accuracy degradation caused by multicollinearity. This

also explains why the HS + TIR combination achieved such strong performance: hyperspectral data capture subtle canopy biochemical and structural responses, whereas TIR data directly reflect the temperature consequences of evapotranspiration and water stress. Their complementary use fundamentally improves the characterization of both vegetation status and surface energy balance. Even when using HS data alone, the models still exhibited strong predictive capabilities. This is closely related to the novel two-band and three-band spectral indices constructed from the 150 available HS bands, which provided critical additional key information for SMC prediction [18].

Specifically, RI and NDI exhibited outstanding predictive performance for different soil depths, particularly after the heading and flowering stages of winter wheat (22 April). This indicates that these indices, through systematic screening of all band combinations, can capture spectral features closely related to SMC. It was found that indices such as DI, RI, NDI, and PI included bands from the visible and red-edge regions, which were highly correlated with SMC. The red-edge region reflects the physiological status of wheat cell surfaces during growth, while the green band in the visible region is closely related to chlorophyll content. The strong correlation between vegetation health, water status, and the red-green spectral bands has also been widely confirmed [46].

In addition, the consistently superior estimation accuracy for the 0–20 cm layer relative to the 20–40 cm layer is physically reasonable. Shallow soil moisture is directly coupled with canopy temperature, shortwave reflectance, and near-surface water exchange, whereas deeper-layer moisture is sensed more indirectly through crop physiological adjustments and soil–plant water transfer processes. Similar depth-dependent behavior has been widely reported in recent winter wheat and multimodal UAV studies [42,43]. In the construction of novel three-band indices, broader spectral coverage clearly enhanced index sensitivity to SMC. For instance, the index B484/(B496 + B680) showed the highest correlation in the 0–20 cm layer, while B546/(B693 + B706) was most effective for the 20–40 cm layer. This aligns with findings in spectroscopic studies regarding specific water absorption features [18]. Ultimately, SHAP analysis revealed that TVDI and the newly developed spectral indices dominated model decisions, indicating that the predictive advantage of the optimal model stems from the synergistic interaction between thermal stress indicators and water-sensitive hyperspectral combinations.

4.2. Prediction Accuracy and Performance Evaluation of TPOT, AutoGluon, H2O AutoML, and FLAML Models

Among the four evaluated AutoML frameworks, H2O AutoML achieved the best and most stable performance across the majority of input scenarios. Its primary advantage lies not only in reaching a higher peak accuracy but also in maintaining robust prediction behavior when handling heterogeneous multimodal predictors. This superiority is primarily attributed to its advanced Stacked Ensemble strategy. Compared with conventional baseline models, H2O AutoML maintained a distinct advantage even under the stricter LOFDO validation. This suggests that its predictive power extends beyond simple random interpolation within mixed samples, demonstrating a reliable degree of temporal transferability within the study area and growing season.

Unlike traditional single learners, which are often sensitive to initial weights, redundant predictors, or high-dimensional spaces, H2O AutoML dynamically integrates the prediction results of base learners (such as GBM, DL, and DRF) by training a metalearner [37]. Mathematically, this strategy effectively reduces the variance and bias of single algorithms, enabling it to maintain the narrowest error distribution even when facing multi-source heterogeneous data containing noise (e.g., RGB redundant features) (Figure 11). In contrast, although the TPOT algorithm, based on genetic programming, theoretically possesses global optimization capabilities, it exhibits instability in high-dimensional complex feature

spaces and is prone to premature convergence or overfitting [13]. This explains why TPOT was found to be the most sensitive to the feature redundancy introduced by RGB data. From a broader methodological perspective, recent literature emphasizes that AutoML enhances modeling efficiency by automating algorithm selection, hyperparameter tuning, and ensemble construction [47,48]. These capabilities are particularly valuable in studies like ours, where the predictor set includes texture variables, thermal indicators, and multiple families of hyperspectral indices with complex nonlinear interactions. In such scenarios, AutoML provides a practical means to explore algorithmic combinations that would be time-consuming and difficult to optimize manually.

Furthermore, the SHAP-based interpretability analysis further validated the physical rationality of the model's decisions. The feature importance ranking showed that TVDI and the novel three-band indices occupied a dominant position in model decision-making, while the contribution of texture features was relatively low. That is, the energy balance reflected by TVDI acts as the primary driving force for inferring root-zone moisture [49], while biochemical variations reflected by spectral indices provide key auxiliary information [50]. It is important to note that AutoML does not replace physical understanding; rather, it serves as an efficient optimization strategy when combined with physically meaningful variables and rigorous validation. Recent studies emphasize that AutoML performance strongly depends on the predefined search space, validation schemes, and data quality [47,48,51]. Therefore, the advantage of H2O AutoML in this study should be interpreted as the outcome of both the AutoML framework and the high-quality multimodal feature design, rather than as evidence that AutoML universally outperforms all conventional machine learning methods under all conditions. While the data-driven model does not explicitly simulate physical processes, its decisions are highly consistent with established biophysical mechanisms governing the Soil–Plant-Atmosphere Continuum (SPAC) [52]. The dominant variables identified by SHAP—specifically TVDI and water-sensitive hyperspectral indices—have clear agronomic and biophysical relevance. This consistency between model reliance and known biological mechanisms suggests that H2O AutoML is not merely fitting arbitrary statistical correlations, but is capturing relationships that are physically plausible in the context of crop water stress and soil–plant–atmosphere interactions.

4.3. Limitations and Future Perspectives on Soil Moisture Content Prediction

Although this study demonstrated that integrating multimodal UAV-based remote sensing data significantly enhances SMC prediction accuracy, several limitations must be acknowledged. First, the current dataset was derived from a single growing season and one specific study area. While the evaluation included both random five-fold and time-independent (LOFDO) validations, the results primarily reflect temporal transferability within the site rather than full spatial or interannual generalization. Second, although the 0.4 m buffer-based averaging strategy helped mitigate local heterogeneity, canopy shadows, and pixel-level noise, explicit pixel-wise shadow masking was not applied. Third, the framework remains largely empirical, and some uncertainties may still arise from growth-stage-dependent variations in canopy structure and thermal dynamics. The spatial heterogeneity of SMC is influenced by complex factors beyond surface reflectance and temperature, including soil physical properties (e.g., porosity, bulk density, and organic matter content), meteorological conditions, and vegetation cover [53]. Consequently, monitoring SMC using discrete sensor measurements alone may not fully meet the requirements for spatiotemporal continuity in water resource management. Detailed soil physical property data and temporally continuous SMC observations are therefore essential for practical irrigation guidance. To further improve the spatiotemporal resolution of SMC estimation, future research should investigate the mechanisms by which soil physical properties shape the spa-

tial distribution of SMC more comprehensively. Recent work indicates that coupling UAV observations with process-based water balance or hydrological models can substantially improve multi-depth root-zone soil moisture estimation. Such hybrid strategies—coupling physically based hydrology models with data-driven approaches—offer a highly promising direction for enhancing both interpretability and temporal continuity [54,55]. Additionally, future studies could extend SMC retrieval to satellite platforms by integrating multi-source, multi-resolution remote sensing data (e.g., Sentinel-2, Landsat, and MODIS) [56]. This trajectory is supported by recent cross-scale studies demonstrating that UAV observations can serve as an effective bridge between sparse ground sampling and continuous satellite-based regional monitoring [42]. Developing scale-transferable SMC products would better support large-scale monitoring applications. Through these advancements, future research will facilitate the development of robust SMC retrieval techniques, providing a scientific foundation for precision agriculture and sustainable water resource management.

5. Conclusions

In this study, by integrating UAV-mounted HS, TIR, and RGB sensors, a soil moisture retrieval framework based on multi-source remote sensing and automated machine learning was systematically constructed for the key growth stages of winter wheat, achieving high-accuracy retrieval of SMC at two soil depths: 0–20 cm and 20–40 cm. The main conclusions are as follows:

1. Among the constructed novel HS indices, the dual-band index NDI (B566, B693) and the three-band index B484/B496 + B680 showed the highest correlation with SMC in the 0–20 cm soil layer (R = 0.616 and 0.629, respectively).
2. The H2O AutoML model demonstrated the highest accuracy in estimating SMC at different depths, followed by FLAML and AutoGluon. The performance metrics were as follows: R values ranged from 0.43–0.72, 0.27–0.63, and 0.25–0.66; RMSE ranges were 1.99–2.96%, 2.18–3.20%, and 2.23–3.16%; and rRMSE ranges were 13.6–23.2%, 15.1–25.1%, and 15.4–24.8%, respectively.
3. Among different sensor combinations, the HS + TIR + RGB combination achieved the highest predictive accuracy, followed by HS + TIR. Their R value ranges were 0.61–0.77 and 0.62–0.76; RMSE ranges were 1.99–2.48% and 2.10–2.52%; and rRMSE ranges were 13.6–19.2% and 15.3–20.2%, respectively.

These results indicate that estimating SMC based on UAV multi-modal data combined with machine learning algorithms holds great potential, providing a methodological basis for regional soil moisture monitoring and precision irrigation regulation.

Author Contributions: Conceptualization, D.Z. and C.L.; methodology, C.L. and C.S.; software, D.Z.; validation, S.L., J.E.K., P.Z., H.L. and N.S.; formal analysis, D.Z.; investigation, D.Z., S.L., P.Z., N.S. and H.N.; resources, J.E.K.; data curation, D.Z. and S.L.; writing—original draft preparation, D.Z.; writing—review and editing, C.L., C.S., H.L., N.S. and H.N.; visualization, D.Z.; supervision, C.L.; project administration, C.S.; funding acquisition, C.L. and C.S. All authors have read and agreed to the published version of the manuscript.

Funding: This research was funded by the National Key Research and Development Program of China (2023YFD1900801).

Data Availability Statement: The raw data supporting the conclusions of this article will be made available by the authors, without undue reservation. The data are not publicly available due to copyrights cannot be available.

Conflicts of Interest: The authors declare no conflicts of interest.

References

1. Baumann, F.; He, J.-S.; Schmidt, K.; Kühn, P.; Scholten, T. Pedogenesis, Permafrost, and Soil Moisture as Controlling Factors for Soil Nitrogen and Carbon Contents across the Tibetan Plateau. *Glob. Change Biol.* **2009**, *15*, 3001–3017. [CrossRef]
2. Cheng, M.; Jiao, X.; Liu, Y.; Shao, M.; Yu, X.; Bai, Y.; Wang, Z.; Wang, S.; Tuohuti, N.; Liu, S.; et al. Estimation of Soil Moisture Content under High Maize Canopy Coverage from UAV Multimodal Data and Machine Learning. *Agric. Water Manag.* **2022**, *264*, 107530. [CrossRef]
3. Zhang, Y.; Han, W.; Zhang, H.; Niu, X.; Shao, G. Evaluating Soil Moisture Content under Maize Coverage Using UAV Multimodal Data by Machine Learning Algorithms. *J. Hydrol.* **2023**, *617*, 129086. [CrossRef]
4. Abdulraheem, M.I.; Zhang, W.; Li, S.; Moshayedi, A.J.; Farooque, A.A.; Hu, J. Advancement of Remote Sensing for Soil Measurements and Applications: A Comprehensive Review. *Sustainability* **2023**, *15*, 15444. [CrossRef]
5. Shahabul Alam, M.; Elshorbagy, A. Quantification of the Climate Change-Induced Variations in Intensity–Duration–Frequency Curves in the Canadian Prairies. *J. Hydrol.* **2015**, *527*, 990–1005. [CrossRef]
6. Ge, X.; Ding, J.; Jin, X.; Wang, J.; Chen, X.; Li, X.; Liu, J.; Xie, B. Estimating Agricultural Soil Moisture Content through UAV-Based Hyperspectral Images in the Arid Region. *Remote Sens.* **2021**, *13*, 1562. [CrossRef]
7. Yang, C.; Mao, K.; Guo, Z.; Shi, J.; Bateni, S.M.; Yuan, Z. Review of GNSS-R Technology for Soil Moisture Inversion. *Remote Sens.* **2024**, *16*, 1193. [CrossRef]
8. CYGNSS Level 3 Soil Moisture Version 3.2 | PO.DAAC/JPL/NASA. Available online: https://doi.org/10.5067/CYGNU-L3S32 (accessed on 26 March 2026).
9. Jin, X.; Kumar, L.; Li, Z.; Feng, H.; Xu, X.; Yang, G.; Wang, J. A Review of Data Assimilation of Remote Sensing and Crop Models. *Eur. J. Agron.* **2018**, *92*, 141–152. [CrossRef]
10. Lambertini, A.; Mandanici, E.; Tini, M.A.; Vittuari, L. Technical Challenges for Multi-Temporal and Multi-Sensor Image Processing Surveyed by UAV for Mapping and Monitoring in Precision Agriculture. *Remote Sens.* **2022**, *14*, 4954. [CrossRef]
11. Li, X.; Cheng, G.; Liu, S.; Xiao, Q.; Ma, M.; Jin, R.; Che, T.; Liu, Q.; Wang, W.; Qi, Y.; et al. Heihe Watershed Allied Telemetry Experimental Research (HiWATER): Scientific Objectives and Experimental Design. *Bull. Am. Meteorol. Soc.* **2013**, *94*, 1145–1160. [CrossRef]
12. Yuan, L.; Li, L.; Zhang, T.; Chen, L.; Zhao, J.; Liu, W.; Cheng, L.; Hu, S.; Yang, L.; Wen, M. Improving Soil Moisture Estimation by Identification of NDVI Thresholds Optimization: An Application to the Chinese Loess Plateau. *Remote Sens.* **2021**, *13*, 589. [CrossRef]
13. Babaeian, E.; Paheding, S.; Siddique, N.; Devabhaktuni, V.K.; Tuller, M. Estimation of Root Zone Soil Moisture from Ground and Remotely Sensed Soil Information with Multisensor Data Fusion and Automated Machine Learning. *Remote Sens. Environ.* **2021**, *260*, 112434. [CrossRef]
14. Li, W.; Liu, C.; Yang, Y.; Awais, M.; Li, W.; Ying, P.; Ru, W.; Cheema, M.J.M. A UAV-Aided Prediction System of Soil Moisture Content Relying on Thermal Infrared Remote Sensing. *Int. J. Environ. Sci. Technol.* **2022**, *19*, 9587–9600. [CrossRef]
15. Wu, Z.; Cui, N.; Zhang, W.; Yang, Y.; Gong, D.; Liu, Q.; Zhao, L.; Xing, L.; He, Q.; Zhu, S.; et al. Estimation of Soil Moisture in Drip-Irrigated Citrus Orchards Using Multi-Modal UAV Remote Sensing. *Agric. Water Manag.* **2024**, *302*, 108972. [CrossRef]
16. Ge, X.; Wang, J.; Ding, J.; Cao, X.; Zhang, Z.; Liu, J.; Li, X. Combining UAV-Based Hyperspectral Imagery and Machine Learning Algorithms for Soil Moisture Content Monitoring. *PeerJ* **2019**, *7*, e6926. [CrossRef]
17. Blatchford, M.L.; Mannaerts, C.M.; Zeng, Y.; Nouri, H.; Karimi, P. Status of Accuracy in Remotely Sensed and In-Situ Agricultural Water Productivity Estimates: A Review. *Remote Sens. Environ.* **2019**, *234*, 111413. [CrossRef]
18. Sahoo, R.N.; Ray, S.S.; Manjunath, K.R. Hyperspectral Remote Sensing of Agriculture. *Curr. Sci.* **2015**, *108*, 848–859.
19. Sohrabinia, M.; Rack, W.; Zawar-Reza, P. Soil Moisture Derived Using Two Apparent Thermal Inertia Functions over Canterbury, New Zealand. *J. Appl. Remote Sens.* **2014**, *8*, 083624. [CrossRef]
20. Hassan-Esfahani, L.; Torres-Rua, A.; Jensen, A.; McKee, M. Assessment of Surface Soil Moisture Using High-Resolution Multi-Spectral Imagery and Artificial Neural Networks. *Remote Sens.* **2015**, *7*, 2627–2646. [CrossRef]
21. Lu, F.; Sun, Y.; Hou, F. Using UAV Visible Images to Estimate the Soil Moisture of Steppe. *Water* **2020**, *12*, 2334. [CrossRef]
22. Wu, Z.; Cui, N.; Zhang, W.; Gong, D.; Liu, C.; Liu, Q.; Zheng, S.; Wang, Z.; Zhao, L.; Yang, Y. Inversion of Large-Scale Citrus Soil Moisture Using Multi-Temporal Sentinel-1 and Landsat-8 Data. *Agric. Water Manag.* **2024**, *294*, 108718. [CrossRef]
23. Haralick, R.M.; Shanmugam, K.; Dinstein, I. Textural Features for Image Classification. *IEEE Trans. Syst. Man Cybern.* **1973**, *SMC-3*, 610–621. [CrossRef]
24. Rallo, G.; Minacapilli, M.; Ciraolo, G.; Provenzano, G. Detecting Crop Water Status in Mature Olive Groves Using Vegetation Spectral Measurements. *Biosyst. Eng.* **2014**, *128*, 52–68. [CrossRef]
25. Nocita, M.; Stevens, A.; Noon, C.; Van Wesemael, B. Prediction of Soil Organic Carbon for Different Levels of Soil Moisture Using Vis-NIR Spectroscopy. *Geoderma* **2013**, *199*, 37–42. [CrossRef]
26. Damm, A.; Paul-Limoges, E.; Haghighi, E.; Simmer, C.; Morsdorf, F.; Schneider, F.D.; Van Der Tol, C.; Migliavacca, M.; Rascher, U. Remote Sensing of Plant-Water Relations: An Overview and Future Perspectives. *J. Plant Physiol.* **2018**, *227*, 3–19. [CrossRef]

27. Mwinuka, P.R.; Mourice, S.K.; Mbungu, W.B.; Mbilinyi, B.P.; Tumbo, S.D.; Schmitter, P. UAV-Based Multispectral Vegetation Indices for Assessing the Interactive Effects of Water and Nitrogen in Irrigated Horticultural Crops Production under Tropical Sub-Humid Conditions: A Case of African Eggplant. *Agric. Water Manag.* **2022**, *266*, 107516. [CrossRef]
28. Ndlovu, M.; Clulow, A.D.; Savage, M.J.; Nhamo, L.; Magidi, J.; Mabhaudhi, T. An Assessment of the Impacts of Climate Variability and Change in KwaZulu-Natal Province, South Africa. *Atmosphere* **2021**, *12*, 427. [CrossRef]
29. Zhang, X.; Zhang, F.; Qi, Y.; Deng, L.; Wang, X.; Yang, S. New Research Methods for Vegetation Information Extraction Based on Visible Light Remote Sensing Images from an Unmanned Aerial Vehicle (UAV). *Int. J. Appl. Earth Obs. Geoinf.* **2019**, *78*, 215–226. [CrossRef]
30. Wang, J.; Ding, J.; Yu, D.; Ma, X.; Zhang, Z.; Ge, X.; Teng, D.; Li, X.; Liang, J.; Lizaga, I.; et al. Capability of Sentinel-2 MSI Data for Monitoring and Mapping of Soil Salinity in Dry and Wet Seasons in the Ebinur Lake Region, Xinjiang, China. *Geoderma* **2019**, *353*, 172–187. [CrossRef]
31. Sandholt, I.; Rasmussen, K.; Andersen, J. A Simple Interpretation of the Surface Temperature/Vegetation Index Space for Assessment of Surface Moisture Status. *Remote Sens. Environ.* **2002**, *79*, 213–224. [CrossRef]
32. Bai, J.; Yu, Y.; Di, L. Comparison between TVDI and CWSI for Drought Monitoring in the Guanzhong Plain, China. *J. Integr. Agric.* **2017**, *16*, 389–397. [CrossRef]
33. Du, L.; Song, N.; Liu, K.; Hou, J.; Hu, Y.; Zhu, Y.; Wang, X.; Wang, L.; Guo, Y. Comparison of Two Simulation Methods of the Temperature Vegetation Dryness Index (TVDI) for Drought Monitoring in Semi-Arid Regions of China. *Remote Sens.* **2017**, *9*, 177. [CrossRef]
34. Liu, Z.; Shi, X.; Warner, E.; Ge, Y.; Yu, D.; Ni, S.; Wang, H. Relationship between Oriental Migratory Locust Plague and Soil Moisture Extracted from MODIS Data. *Int. J. Appl. Earth Obs. Geoinf.* **2008**, *10*, 84–91. [CrossRef]
35. Olson, R.S.; Moore, J.H. TPOT: A Tree-Based Pipeline Optimization Tool for Automating Machine Learning. In *Proceedings of the Workshop on Automatic Machine Learning*; PMLR: New York, NY, USA, 2016; pp. 66–74.
36. Erickson, N.; Mueller, J.; Shirkov, A.; Zhang, H.; Larroy, P.; Li, M.; Smola, A. AutoGluon-Tabular: Robust and Accurate AutoML for Structured Data. *arXiv* **2020**, arXiv:2003.06505.
37. LeDell, E.; Poirier, S. H2O AutoML: Scalable Automatic Machine Learning. In Proceedings of the AutoML Workshop at ICML, Virtual, 18 July 2020.
38. Wang, C.; Wu, Q.; Weimer, M.; Zhu, E. FLAML: A Fast and Lightweight AutoML Library. *Proc. Mach. Learn. Syst.* **2021**, *3*, 434–447.
39. Jin, X.; Li, Z.; Feng, H.; Ren, Z.; Li, S. Deep Neural Network Algorithm for Estimating Maize Biomass Based on Simulated Sentinel 2A Vegetation Indices and Leaf Area Index. *Crop J.* **2020**, *8*, 87–97. [CrossRef]
40. Rischbeck, P.; Elsayed, S.; Mistele, B.; Barmeier, G.; Heil, K.; Schmidhalter, U. Data Fusion of Spectral, Thermal and Canopy Height Parameters for Improved Yield Prediction of Drought Stressed Spring Barley. *Eur. J. Agron.* **2016**, *78*, 44–59. [CrossRef]
41. Zhang, L.; Liu, Y.; Ren, L.; Teuling, A.J.; Zhang, X.; Jiang, S.; Yang, X.; Wei, L.; Zhong, F.; Zheng, L. Reconstruction of ESA CCI Satellite-Derived Soil Moisture Using an Artificial Neural Network Technology. *Sci. Total Environ.* **2021**, *782*, 146602. [CrossRef]
42. Yu, X.; Yin, Q.; Qian, L.; Zhang, C.; Shao, L.; Ran, D.; Wang, W.; Zhang, B.; Hu, X. Cross-Scale Soil Moisture Content Monitoring of Winter Wheat by Integrating UAV and Sentinel-1/2 Data. *Agric. Water Manag.* **2025**, *320*, 109831. [CrossRef]
43. Vahidi, M.; Shafian, S.; Frame, W.H. Multi-Modal Sensing for Soil Moisture Mapping: Integrating Drone-Based Ground Penetrating Radar and RGB-Thermal Imaging with Deep Learning. *Comput. Electron. Agric.* **2025**, *236*, 110423. [CrossRef]
44. Chu, C.; Ma, Z.; Li, Z.; Hu, Y.; Li, T.; Zhao, J.; Li, J.; Li, X.; Wang, Z.; Wu, W. Enhancing Multi-Stage and Multi-Depth Soil Moisture Estimation in Winter Wheat Fields with UAV Remote Sensing Fusion and Ensemble Learning Strategy. *Ecol. Indic.* **2026**, *183*, 114651. [CrossRef]
45. Zhang, L.; Niu, Y.; Zhang, H.; Han, W.; Li, G.; Tang, J.; Peng, X. Maize Canopy Temperature Extracted From UAV Thermal and RGB Imagery and Its Application in Water Stress Monitoring. *Front. Plant Sci.* **2019**, *10*, 1270. [CrossRef]
46. Kullberg, E.G.; DeJonge, K.C.; Chávez, J.L. Evaluation of Thermal Remote Sensing Indices to Estimate Crop Evapotranspiration Coefficients. *Agric. Water Manag.* **2017**, *179*, 64–73. [CrossRef]
47. Salehin, I.; Islam, M.S.; Saha, P.; Noman, S.M.; Tuni, A.; Hasan, M.M.; Baten, M.A. AutoML: A Systematic Review on Automated Machine Learning with Neural Architecture Search. *J. Inf. Intell.* **2024**, *2*, 52–81. [CrossRef]
48. Baratchi, M.; Wang, C.; Limmer, S.; van Rijn, J.N.; Hoos, H.; Bäck, T.; Olhofer, M. Automated Machine Learning: Past, Present and Future. *Artif. Intell. Rev.* **2024**, *57*, 122. [CrossRef]
49. Shi, J.; Wang, J.; Hsu, A.Y.; O'Neill, P.E.; Engman, E.T. Estimation of Bare Surface Soil Moisture and Surface Roughness Parameter Using L-Band SAR Image Data. *IEEE Trans. Geosci. Remote Sens.* **1997**, *35*, 1254–1266. [CrossRef]
50. Thenkabail, P.S.; Smith, R.B.; De Pauw, E. Hyperspectral Vegetation Indices and Their Relationships with Agricultural Crop Characteristics. *Remote Sens. Environ.* **2000**, *71*, 158–182. [CrossRef]
51. Kim, N.; Lee, S.-J.; Sohn, E.; Kim, M.; Seong, S.; Kim, S.H.; Lee, Y. An Automated Machine Learning Approach to the Retrieval of Daily Soil Moisture in South Korea Using Satellite Images, Meteorological Data, and Digital Elevation Model. *Water* **2024**, *16*, 2661. [CrossRef]

52. Manzoni, S.; Vico, G.; Porporato, A.; Katul, G. Biological Constraints on Water Transport in the Soil–Plant–Atmosphere System. *Adv. Water Resour.* **2013**, *51*, 292–304. [CrossRef]
53. Wang, S.; Li, R.; Wu, Y.; Wang, W. Estimation of Surface Soil Moisture by Combining a Structural Equation Model and an Artificial Neural Network (SEM-ANN). *Sci. Total Environ.* **2023**, *876*, 162558. [CrossRef] [PubMed]
54. Reichstein, M.; Camps-Valls, G.; Stevens, B.; Jung, M.; Denzler, J.; Carvalhais, N. Prabhat Deep Learning and Process Understanding for Data-Driven Earth System Science. *Nature* **2019**, *566*, 195–204. [CrossRef] [PubMed]
55. Wang, J.; Huang, H.; Ariyasena, H.H.S.; Zhao, J.; Zhang, X.; Gao, X.; Zhao, X.; Zhao, Y. A UAV-Based Method for Root Zone Soil Moisture Modeling of Different Farmland Scale with Grain and Economic Crops. *Agric. Water Manag.* **2025**, *321*, 109932. [CrossRef]
56. Mohanty, B.P.; Cosh, M.H.; Lakshmi, V.; Montzka, C. Soil Moisture Remote Sensing: State-of-the-Science. *Vadose Zone J.* **2017**, *16*, vzj2016.10.0105. [CrossRef]

Disclaimer/Publisher's Note: The statements, opinions and data contained in all publications are solely those of the individual author(s) and contributor(s) and not of MDPI and/or the editor(s). MDPI and/or the editor(s) disclaim responsibility for any injury to people or property resulting from any ideas, methods, instructions or products referred to in the content.